Honors College

Spring 5-2016

Optimization and Synthesis of Silver Nanoparticles Embedded Within a Porous Substrate for Raman Spectroscopy

Matthew W. Talbot
University of Maine

Recommended Citation

OPTIMIZATION AND SYNTHESIS OF SILVER NANOPARTICLES EMBEDDED

WITHIN A POROUS SUBSTRATE FOR RAMAN SPECTROSCOPY

by

Matthew W. Talbot

A Thesis Submitted in Partial Fulfillment
Of the Requirements for a Degree with Honors
(Bioengineering)

The Honors College

University of Maine

2016

Advisory Committee:
    Michael D. Mason, Ph. D, Professor of Chemical and Bio. Engineering, Advisor
    Sara L. Walton, Ph.D, Professor of Chemical and Biological Engineering
    William M. Gramlich, Ph.D, Professor of Chemistry
    Douglas W. Bousfield, Ph. D, Professor of Chemical and Biological Engineering
    Sarah Harlan-Haughey, Ph. D, Professor of English and Honors

ABSTRACT:

Raman spectroscopy is a promising method for detection of a wide range of water contaminants. Raman spectroscopy's growing list of applications relies upon signal enhancement achieved in recent years. A test strip or substrate designed to optimize Raman spectra, capable of withholding water and enhancing signal, would be a useful tool for applications including water quality tests. Signal enhancement may be achieved by the addition of silver nanoparticles (NPs) into a three-dimensional structure of cellulose nanofibers (CNF). The magnitude of signal enhancement may be related to nanoparticle size and morphology, and so control over the synthesis of silver nanoparticles could prove essential to this emerging technology. Particle diameter may be controlled by careful selection and concentration adjustment of the reducing agent in addition to varying the reaction's duration. In addition to the resulting size, the reliability of the signal would rely upon its reproducibility, which would in turn be affected by the size distribution of nanoparticles produced, as well as their even dispersion within the test strip. To produce a nanoparticle engineered for use within a cellulose nanofiber substrate, a number of these parameters were investigated.

ACKNOWLEDGEMENTS:

Table of Contents

Table of Figures:

Table of Tables and Equations:

Chapter 1: Introduction

Potable water is estimated to be a concern for over 2 billion people worldwide. The World Health Organization reported in 2015 that the number of individuals drinking from water containing feces was more than 1.8 billion, and of these 660 million were relying on water from unimproved sources, i.e. naturally occurring water sources without any man-made improvements [1, 2]. Figure 1 shows the extent to which the global population is subjected to drinking from unsafe sources. In countries highlighted in black, less than 50% of the population had access to reliable, safe water [1]. Consequently, over a half million people died from diarrhea after consuming water containing bacteria or vectors which lead to diseases including cholera, dysentery, and typhoid [1, 2].
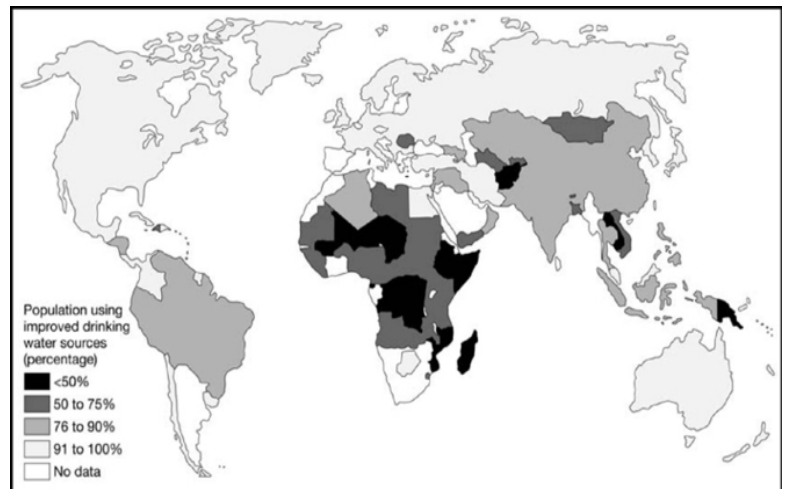
Figure 1: Worldwide drinking water quality [1]

Lack of access to safe water due to economic reasons (i.e. an African village without the capabilities or resources to purchase a water quality test) has been reduced, but has far from been eliminated. It is estimated that to prevent sickness, healthy adults require up to 50 liters each day for drinking and bathing water, a volume not currently met by 50% of the population in over 47 countries worldwide [1].

A consistent, cheap, and portable device for optically analyzing water samples would provide a large population of the world with the ability to test for a wide range of

known water contaminants. This would potentially prevent spread of disease, and indicate demand for water purification given knowledge of potential safety concerns or lack thereof for local water supplies [2].

Three routes that would make use of the same chemical processes were considered for determining if a water source contains pollutants. The first was direct detection, in which the pollutant itself is detected through chemical processes. An example of this technique may be the combination of high performance liquid chromatography and high resolution mass spectrometry (HPLC-HRMS) technologies, for which detection of target products relies upon large test volumes over time [3]. It is costly and careful sample preparation considerations. A second route for determination of water safety relies upon the reaction chemistry in that an intermediate or associated compound to the pollutant must be degradable, and capable for use in identification of the larger group of hazardous chemical products. This could also involve a similar chemical process, but as the chemicals might be found in higher concentration, there is a greater margin for the detection limit [3]. Finally, testing for a select few target molecules, which are proven to commonly arise in contaminated water supplies, may be utilized [3]. This method may be applied to a potable water test featuring Raman spectroscopy, the method chosen for this project. Raman spectroscopy with enhanced signal is capable of detecting a wide range of molecules [4]. However, Raman devices are incapable of detecting a number of elemental inorganics and have difficulties generating adequate signal for detection of water, a polar solvent [4, 5, 6].

Organic molecules are targeted specifically due to their increased contamination levels caused by hazard-containing waste and by-product producing materials including

fertilizers, herbicides, i.e. glyphosate, surfactants including perfluorinated compounds, pharmaceuticals, flame retardants, and by-products of disinfectants, i.e. haloacetic acids [2, 3]. In rapidly developing countries, mismanagement of resources has led to serious pollution of water supplies. For instance, India and China have seen remarkable agricultural growth over the past century, but are severely lacking the regulations and laws present in many Western countries such as the United States. This leads to the presence of harmful chemicals in water supplies downstream from agricultural crops, due to runoff [2]. To compete with other emerging technologies, the detection limit of these organics would need to be equal to or less than a few nanograms per liter [3]. Importantly, Raman is also capable of detecting most human and biological wastes, as proteins and nucleic acids critical to life have distinct peaks [4].

Raman spectra are considered to be unique to molecules, providing a "fingerprint" from sample contents that may be used to accurately and consistently detect the presence of numerous molecules [4, 5]. Surface-enhanced Raman spectroscopy (SERS) was chosen for its improved signal and its specificity, practicality, and lack of bleaching or damage to samples [5]. This technique is inexpensive relative to mass spectroscopy, high power liquid chromatography, and fluorescence spectroscopy (fluorometry) [7]. Infrared spectroscopy is a poor choice for tests of water due to a large hydroxyl peak corresponding to water, which makes distinguishing potential peaks within the same region impossible [6]. Many of these techniques, in addition to currently not being as economically feasible for the desired level of widespread use as Raman spectroscopy, may require knowledge to maintain and operate; this would include proper sample preparation and machine maintenance. The potential for a portable Raman test is a

significant benefit, as well as the lack of significant sample preparation, which is needed with chemical techniques such as mass spectroscopy [5]. The necessary components of a Raman setup could be scaled down to a relatively inexpensive handheld device [8]. Of the many optical methods available, it was determined that Raman spectroscopy was best suited to the desired application.

Although Raman spectroscopy is an excellent choice, there are serious concerns such as the weak signal generation. To solve this problem, a technique known as surface enhanced Raman spectroscopy may be used [5]. Jiang and Hsieh were successful in SERS signal enhancement through synthesis of silver nanoprisms embedded within cellulose nanofibrils [9]. Sodium borohydride, $NaBH_4$ was used as a reducing agent, and the CNF acted as a capping agent to sterically stop further growth of silver nanostructures. Using Rhodamine 6G dye, the CNF-silver substrate was shown to increase signal intensity by a factor of approximately $5*10^3$ [9].

A gradient in porosity within a strip of CNF was proposed to aid in the transport and wicking of water through the hydrophilic, wettable surface microcapillaries. Water may travel slowly through into the bulk, aided significantly by hydrogen bonding and the adhesive and cohesive forces, and driven by the pressure gradient. Molecules will concentrate at the contact surface between the CNF composite matrix and aqueous solution, as hydrophobic analyte interacts with the carbon backbone of cellulose. As seen in Figure 2, the desired composite matrix has a porous surface into which analyte-containing water will flow as sample

Figure 2: Model Porous Test Strip made within Solidworks CAD, pores not to scale

is added directly to this surface. On this porous surface the pollutants may be found even after the water is drawn by capillary action into the bulk of the test strip. This area of composite matrix will be targeted with the laser for Raman detection, and should have silver nanoparticles present at a sufficiently high concentration and properly dispersed. This would ensure the local enhancement effects of SERS are capable of reliably detecting pollutant concentration. Long term stability of the silver nanoparticle and CNF system (composite matrix) is essential for this to be a feasible solution for reaching third world communities.

Although implementation of any water quality testing discussed would require a sizeable initial investment, it is foreseeable that the test strips discussed could be made to be remarkably inexpensive. Chemicals for silver nanoparticle synthesis are inexpensive, the synthesis process is not overly involved, and CNF is made of cellulose, the most abundant polymer in the world [10]. Synthesis of these substrates would also not necessarily involve processes requiring long time durations, or more than 7 days [10]. CNF would also have the added benefit of being a disposable material. The disposability of silver nanoparticles is debatable; studies have largely proven their cytotoxicity to bacteria, though at the concentrations within a CNF composite matrix they would likely pose no health threat to animals [8]. The relative simplicity and low cost make the proposed substrates an excellent candidate for one-use disposables, provided some care may be taken with the disposal of silver nanoparticles.

This paper details work done to create a stable, highly reproducible substrate of porous cellulose nanofiber embedded with evenly-dispersed silver nanoparticles for water quality testing utilizing Raman spectroscopy. Work focused upon producing

monodisperse, or similar size, silver NPs of desired size range and adjusting solution pH for improved entrainment and surface interaction within cellulose nanofibrils, as well as potentially greater signal enhancement in future tests.

Chapter 2: Background and Theories

2.1: Raman Spectrophotometry

Raman spectroscopy has become increasingly utilized in recent years for biological applications [4]. It requires minimal equipment to track chemical and biological changes in real-time [4]. Portable Raman setups are feasible, and cost-effective relative to other methods of testing the chemical state of a biological system; ReporteR, TruScan, and Tellspec are all currently available portable Raman spectrometers [8].

Raman spectroscopy measures the vibrational, rotational, and near-infrared modes of a molecule through detection of changes in energy, or corresponding frequency, (10-10,000 cm^{-1}) in scattered light [7, 8]. The light scattering is directly related to polarizability, which is a function of how tightly a molecule holds its electrons [7]. The orientation and ordered structure of bonds, levels of hydrogen bonding, molecular symmetry, and atomic weights within a sample affect the generated Raman spectra [8].

In the presence of an electromagnetic field, the electron cloud of a molecule may experience a change [8]. The incident laser provides the electromagnetic field, and upon interaction with molecular vibrations, a change in the electron cloud is measured when the laser's frequency shift is determined by a detector [8]. As shown by Equation 1, the polarizability (α), and intensity of the electric field (*E)*, are related to the induced electric dipole moment of a molecule, (*P)*, by the equation,

$$P = \alpha E$$

Consequently the laser source and power must be chosen to fit the signal needs as the electric field is controlled by the intensity of electromagnetic radiation, the light emitted. Moreover, the wavelength, typically of monochromatic or single wavelength light, at which the light source emits may be an important decision depending upon the desired application as a specific wavelength may be chosen corresponding to a frequency value at which a target's electrons resonate, increasing signal [8].

A beam of laser light contacting sample may experience a lasting change in energy, E, and corresponding wavelength, λ, and frequency, *v*. The velocity of light in a vacuum, c, and Plank's constant, h, complete the relationship given by Equation 2,

$$E = \frac{hc}{\lambda} = hv$$

Equation 2: Einstein Photoelectric Effect

This change is known as a Stokes shift if the photon loses energy and increases in frequency, and anti-Stokes shift if energy is gained while frequency lost [5, 8]. This means that with a molecule's return from the virtual or excited state induced by excitation by a laser light source, the Stokes shift will see energy absorbed by the molecule, and lost from the
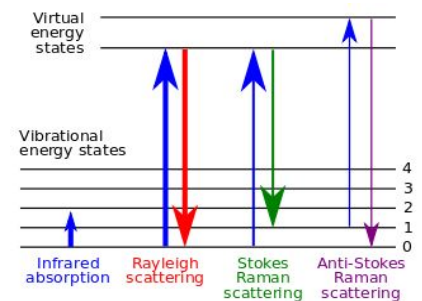
Figure 3: Energy state diagram for Raman shift, Rayleigh scattering, and IR

photon. Thus the molecule returns to a rotational energy state higher than that at which it was previously, as seen in Figure 3 [8]. The photons emitted are then read by a detector. Rayleigh scattering is the term for when a molecule experiences a virtual energy state

upon laser excitation only to return to its original energy state [5]. Rayleigh scattering confers no information of the system to the detector, as it is the emitted light is at the wavelength and frequency corresponding to the light source itself rather than signal indicating a change in energy upon the molecule leaving the virtual state. This is shown in Figure 3 as the red arrow returns to the ground state [5]. Rayleigh scattering is called elastic scattering, while both Stokes and anti-Stokes are inelastic scattering [5].

Raman spectra often exhibit a 99% reduction in the intensity of laser light [11]. Less than 1% of photons emitted by the light source experience Raman scattering by the sample and reach the detector; Rayleigh scattering dominates. [11]. Over time this mode of spectroscopy has drastically been improved, broadening its uses to include biology [4]. Intensity of scattered light $I_{scattered}$, or Mie scattering taken at the Rayleigh limit for resolution is given by Equation 3,

$$I_{Scattered} \propto \frac{r^6}{\lambda^4} \left| \frac{m-1}{m+2} \right|^2$$

Equation 3: Light Scattering

where m is a factor that encompasses molecular properties and confers the refractive indexes of both molecule and surrounding media or solvent, r is radius of the molecular cross-section, and wavelength is given by λ.

Li et al. indicate the necessity of a standard dye from which to base all other spectra [6]. The nature of the optical setup may give rise to significant changes in spectra intensity due to seemingly minor changes in the laser source used, laser intensity, and positioning [5, 6]. Raman spectra relative to a standard may be used to understand the

system, done through comparison to a known concentration of standard within the same sample or to the standard externally for relative peak location [6]. Due to the relativistic nature of Raman spectra, intensity is given in arbitrary units, a.u. Conveniently, if done properly, a molecule's Raman spectra intensity is directly proportional to its concentration [6]. Spectra are plotted with the intensity of inelastically scattered light (arb. units, AU, or a.u.) as the dependent variable and the Raman shift from the incident laser source, given as a frequency, or wavenumber (cm^{-1}), as the independent variable [6].

2.2: Surface Enhanced Raman Spectroscopy (SERS)

In 1997, detection of a single crystal violet molecule was achieved [8]. This was possible because of techniques such as SERS, or surface-enhanced Raman spectroscopy. SERS was developed to increase the intensity of Raman spectra through polarizability and increased electromagnetic field of a molecule with the local surface plasmon resonance effect [5]. Provided a molecule is capable of experiencing a change in polarization and is located between two metallic nanoparticles, the effective electromagnetic field often experiences an increase as electrons at a region of the nanoparticle's surface oscillate in resonance with the laser frequency [8]. The strength of the oscillation of electrons in gold and silver nanoparticles at a laser source frequency is rather unique [8].

The LSPR effect is most intense at wavelengths corresponding to values across the shoulder of the nanoparticle absorbance peak; the frequency at which the laser source emits light and the frequency corresponding to the peak absorbance intensity for silver or gold nanoparticles do not have to be perfectly aligned [8]. The monochromatic

wavelength of the laser source used in this project emits light at a wavelength of 532 nm, and the peak absorbance intensity for most silver nanoparticles is between 400-470 nm. The SERS effect for a 532 nm laser source produced by silver nanoparticles was still found to be at a satisfactory value, as signal enhancement through SERS was shown to increase spectra intensity by a factor of approximately 10^{10} in tests of dilute crystal violet solutions.

Enhancement on the order of 10^6-10^8 has been reported for systems optimized to increase signal strength [8]. If properly aligned between two nanoparticles, electromagnetic enhancement goes by E^4, while the chemical enhancement is approximately 10^2 [8]. This electromagnetic enhancement appears to rely heavily upon position between two nanoparticles; that is to say that without both nanoparticles creating a "hotspot" and only one nanoparticle in the nanoscale vicinity of an analyte, the enhancement would be less than E^2 [5].

The surface plasmon excitation of valence electrons in resonance with the laser increases the localized electric field, is the electromagnetic mode of enhancement [8]. Chemical enhancement is responsible for the increased change in polarizability [8]. At least three modes of this chemical enhancement were proposed: ground state chemical enhancement, resonance Raman enhancement, and charge-transfer resonance [8]. Ground state chemical enhancement is due to an alteration in the distribution of target molecule's electron cloud because of the metal's presence [8]. Resonance Raman is possible when a new electronic state is generated resonating at the laser's frequency [8]. This new state is the result of covalent bonding between target molecules and either the NP or ions. Charge-transfer resonance relies upon a charge transfer and the difference in Fermi

Energy of metal and analyte [8]. The difference in energies of the metal and the highest occupied molecular orbital (HOMO) or lowest unoccupied molecular orbital (LUMO) of analyte must match that of the laser [8]. As a result signal is enhanced provided the wavelength is in resonance with charge-transfer transitions [8].

$$\varepsilon(\lambda) = \varepsilon_r(\lambda) + i\varepsilon_i(\lambda); m = n + ik, m = \sqrt{\varepsilon}$$

Equation 4: Dielectric Relationships and LSPR

$$E(\lambda) \propto \frac{\varepsilon_i(\lambda)}{(\varepsilon_r(\lambda) + \chi\varepsilon_{med})^2 + \varepsilon_i(\lambda)^2}$$

Equation 5: Solution of Maxwell's Equations for spheroid metallic NP

The electric field is dependent upon the dielectric constant of the NP [8]. The dielectric constant ε in Equation 4 of silver nanoparticles is approximately 10-100 times greater than gold, making silver a better choice for SERS applications in this respect [8]. Equation 4, the dielectric constant, will determine the localized surface plasmon resonance; the square of refractive index is also equal to this quantity. It also shows that the refractive index may be related to the absorption coefficient of the nanoparticles k. The extinction as a function of wavelength and the dielectrics of a particle is shown by Equation 5. χ relates the nanoparticle shape into the equation, or the aspect ratio [8]. The geometry of all nanoparticles synthesized by the methods attempted would in theory have values for this constant approaching 1. This one may infer from TEM and SEM images, as the majority of particles appear spherical, which is necessary for accuracy of Mie theory approximation.

It was hypothesized that to optimize signal enhancement, a balance between nanoparticle stability, dispersion, and size must be reached.
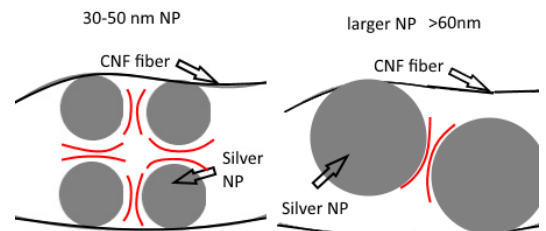
Figure 4: Optimization of Silver NP size and dispersion within pores

Particles of 100 nm size ranges may present large gaps when entrained within fibers, whereas 30-50 nm particles would allow for the enhancement in multiple directions. As illustrated in Figure 4 the predicted model is one in which mid-range nanoparticles, shown in the left image, create a greater effective surface area of enhancement, whereas the larger nanoparticles in the depiction to the right do not enhance the field for as large a volume of space within the CNF matrix. Red lines are used in this illustration to propose areas experiencing surface enhancement.

2.3: Silver Nanoparticles

Nanoparticles are typically defined as a particle ranging from 1 to 100 nm [8]. Colloidal silver contains silver particles, typically stably suspended in solution, of which each silver particle is comprised of 1000-58000 silver atoms [8]. Silver nanoparticles are of particular interest due to their electrical and chemical properties. Silver nanoparticles have been used extensively for their antimicrobial activity, [4, 8] and similar silver nanoparticle-loaded microporous structures to those made in this paper were investigated for this application [8]. As the size of silver nanoparticles is believed to be of great importance to its functionality as an antimicrobial [8], work done in this paper may be used in future development of this technology.

As a noble metal, silver is inert and its valence shell of electrons is near completing its full octet [12]. As a result of the octet rule, oxidation-reduction reactions are energetically favorable upon ionic separation of an insoluble silver salt in solution [12]. Of additional significance are silver's electronic and chemical properties for use in Raman spectroscopy. Silver and gold nanoparticles both exhibit surface resonance at wavelengths within the visible spectrum [8]. This is excellent for Raman, as the

resonance frequencies may be aligned closely with the laser wavelength used. Ideally the SERS substrates created produce the greatest increase in electronic resonance. Silver may not hold its electrons as tightly as gold, making enhancement by electronic oscillation, delocalized electrons [5]. Silver is also less expensive than gold.

There is potential for formation of silver oxide with similar methods of reduction in making silver nanospheres detailed in the paper [13]. Silver oxide would not be ideal for Raman spectroscopy, as the structure is lacking in electron cloud delocalization [13]. As such, future work may involve taking x-ray diffraction readings to test for the presence of these unwanted silver structures.

2.4: Why Cellulose Nanofibers

Cellulose is a polysaccharide, or polymer, made of sugar subunits. D-glucose is connected by β(1→4) linkages in long chains [7, 14]. It is the most abundant polymer in the world, making mass production of cellulosic products feasible and potentially inexpensive [15]. At the University of Maine Pilot Plant facility, 1 ton of 3 wt% cellulose nanofibril slurry can be produced in a day using the mass colloider, which creates forces capable of separating pulp into cellulose nanofibrils (CNF) [16]. Some analysts anticipate the market for cellulose nanofibers to reach as high as $8 billion by 2030 [15], a figure that indicates future growth in production of CNF and consequently the potential for lowered cost.

Cellulose nanofibrils were chosen for the substrate into which silver nanoparticles were embedded. CNF is made of long fibers, or long strings of cellulose [17]. The desired material would exhibit roughness on the bulk surface [5], for which cellulose nanofibers

are well suited. Silver nanoparticles and biomolecules alike may associate with or are trapped in the many strings of cellulosic fibrils as the largely hydrophilic polymer is wetted with sample. As a material with hydrophilic groups, cellulose forms hydrogen bonds with water molecules, and solution is brought into the composite matrices by capillary action. Soluble molecules are brought along with the water.

Cellulose nanocrystals were also considered for use as a polymer substrate. The structure of individual CNCs is described as similar to crystalline needles several hundred nanometers in length and 10-20nm in width [17]. During the synthesis of CNC, acid removes most amorphous moieties, leaving a highly crystalline product [18]. The 3D structure of CNC is structurally weak, composed of thin layered sheets [17, 18]. As such, CNF is capable of withstanding greater compressive forces than CNC at equal volume percentages greater than 1.5%, or porosities less than 98.5% [17]. At a value of 94% porosity of CNF, the Young's Modulus for CNF is nearly 3 times that of CNC, approximately 2100 GPa compared to 800 GPa [17]. It is believed that the final porosity desired for use as a composite matrix for Raman spectroscopy is lower than those values tested for compressive strength within the literature. Extrapolating from the trend in literature values, it appears as though the Young's modulus value for CNF continues to increase relative to that of CNC, suggesting CNF is a significantly more durable material. Although the CNF composite matrices at porosities utilized for the Raman SERS effect may not be considered conventionally strong materials, they are not as prone to crumbling upon handling as with CNC composite matrices. CNC may be quasi-isotropic, or have a similar layered sheet structure in two dimensions [18], a feature beneficial for reproducible readings, but ultimately CNC does not offer the material strength of CNF.

The porous structure of designed substrates was possible by controlled removal of water from CNF by a pressure drop across porous bricks in which the CNF dries. The Hagen-Poiseuille Law, Equation 6, can be used to describe fluid flow through a rigid, single, circular microscale pipe [19]. Equation 7 describes the flow through a porous media with its own permeability, Darcy's Law, which is derived from Poiseuille's Law [20]. The permeability factor, or hydraulic conductivity, describes the tortuosity, or degree to which the pores are misshapen or have bends [20].

$$Q = \frac{\Delta P \pi R^4}{8 \mu L} \qquad\qquad Q = -k \nabla \varphi$$

Equation 6: Poiseuille's Law   **Equation 7: Darcy's Law**

The rate of water removal, and thus the rate of porosity change, is dominated by the capillary forces of the porous blocks which make up the drying setup. Blocks are added to the top of the drying slurry after approximately 2 hours, providing weight needed to expedite the drying process and ensure the CNF density was sufficient.

The "skin", or more dense and low porosity CNF near each of the drying setup's 6 sides, is more exposed as it is in contact with the porous blocks. The skin forms a more ordered structure with increased levels of hydrogen bonding density. All water lost from CNF exits through the outer layer of CNF in contact with the blocks of the drying setup. Smaller pores result, as water near the surface has less distance to travel and is more likely to exit through the porous blocks than water near the CNF center, which has farther to travel and does not as strongly "feel" the capillary forces generated by the porous blocks.

An aerogel is an air solid colloid [21]. Following removal from the drying setup, the substrate is made into an aerogel. The water is frozen by liquid nitrogen to ice-template, or preserve structure, and then sublimated in a freeze dryer to remove it. These aerogels are stable and it is in this form that Raman spectra and final porosity measurements are taken.

2.5: Colloidal Chemistry

The colloidal stability, or stability of a solution of suspended particles as with the silver NP solution, is governed by electrostatic interactions [21]. Citrate ion adsorbed to a nanoparticle surface in an electrostatic double layer repels aggregation of other particles by repelling the negatively charged surface of the citrate adsorbed nanoparticle [21].

Zeta potential is an indication of stability, as it is an indirect measurement of distance between particles, the mean free path, and the Debye length [21, 22]. Negatively charged citrate ion, or borohydride ion electrostatically attracted to the slightly positive silver nanoparticle surface builds a double layer, repelling similarly coated silver nanoparticles to avoid aggregation [21, 23]. Zeta potential is a measure of the strength of repulsive or attractive charges between particles in solution [21]. At low sodium citrate concentrations, the silver nanoparticle is not fully covered in adsorbed citrate ions [23]. Consequently, if the orientations of nanoparticles are such that negatively charged citrate adsorbed to one nanoparticle surface is attracted to a positively charged "bald spot" on another nanoparticle, the nanoparticles may form an aggregate [23]. This may be prevented by adding citrate until the nanoparticle surface is entirely covered in adsorbed citrate, ensuring the nanoparticles experiences a repulsive force. Addition of too much

sodium citrate will result in a strong screening effect, as sodium ions dampen the strength of the electric field created by the electrostatic double layer [24]. As concentration of positively charged sodium ions increases, the field generated by the negative citrate ions on the nanoparticle surface is felt less in their presence, as field is cancelled and repulsive force lessened [24]. The Debye length is a measure of the distance a particle's charge is felt, and may be used to describe this system [5].

Van der Waals forces are responsible for the clumping of nanoparticles within the CNF composite matrices [12, 21]. Molecules will have a momentary dipole due to the relative position of electrons within the valence shell, as governed by the Pauli Exclusion Principle [7]. This momentary dipole may serve to attract similar molecules. The citrate ion is necessary to prevent aggregates from forming by creating an electrostatically charged double layer such that the attractive London dispersion force from two silver nanoparticles is negligible relative to the electrostatic force of the negatively charged surfaces comprised of citrate ions [21]. The proximity of nanoparticles and the influence of van der Waals forces are thus minimized.

Mean free path refers to the distance a particle must travel before colliding with another particle [21]. It is a function of the number of particles, particle diameter, solution volume, and average particle velocity [22]. During the reaction, particle velocity is affected by the rate of stirring in addition to the thermal noise or Brownian motion of particles, and electrostatic forces at play within the reaction [21]. In the colloidal system without stirring, Brownian motion and electrostatic forces affect the velocity of particles and rate of particle collision. The collision of solvent molecules with particles produces randomized motion that increases with temperature, or thermal energy of the system [21].

pH generally affects affinity for electrons, and may determine if the hydroxyl group of citrate is protonated or deprotonated. Consequently, adjustment of pH may affect the zeta potential and electrostatic charge repelling nanoparticles [23]. Stability will be affected again by how charge is "felt" and the effective repulsion forces; or the Debye length of silver NPs [24].

2.6: Current Methods of Silver Nanoparticle Synthesis

Silver nitrate is an electrolyte, soluble in water, and consequently will dissociate to its ions, as will sodium citrate [12]. Following the octet rule that atoms favor a full valence shell of electrons and this may be achieved through an oxidation-reduction reaction, citrate will act as a reducing agent and donate its electron to silver [12]. Likewise nitrate will do the same and donate its extra electron to sodium, forming an ionic bond [12]. The sodium ion in solution has less of an effect upon the solution than citrate does [23]; a metal with a different charge or electronegativity than sodium could negatively alter the kinetics.

The extent to which these molecules are insoluble in water may be described by the solubility product constant, K_{sp} [12]. Varying levels of insolubility and the extent to which the molecules dissociate in water are different between compounds chosen for synthesis [8, 12]. The solubility constant was considered by Bastús et al. when deciding upon the concentration of reducing agent [25]. Chemical reduction is the most common method of silver nanoparticle synthesis. Insoluble silver salts separate in solution, leaving ionic Ag^+ to be reduced to the ground state Ag^0. This reaction typically occurs within the order of 200ms [12]. Reduction of silver is then followed by nucleation, as small clusters of reduced silver are formed and then collide [8]. As reducing agent and ionic silver are

consumed throughout the reaction, less Ag^0 is produced, so fewer new "seeds" are

formed. This means rather than formation of new Ag^0 dimers, followed by trimers, and

clusters, the Ag^0 is more likely to collide with a larger forming nanoparticle, coalescing,

or aggregating. Coarsening is an intermediate stage that may arise in which small,

nanoscale particles collide, perhaps <5 nm in this context; aggregation will be used to

describe clustering of particles greater than this [21]. The general formation of

nanoparticles may be modeled with Ostwald ripening kinetics,

$$\bar{R}^3 - \bar{R}_0^3 = \frac{8\gamma c_\infty v^2 D}{9RT} t$$

Equation 8: Ostwald Ripening

This relates the average particle radius, (R), to the solubility of the ground state silver

within a nanoparticle, (c_∞), the surface energy (γ), and the diffusion coefficient of the

elemental silver, (D) [21]. Further into the reaction, the rate of new Ag^0 approaches zero

and the particle formation kinetics change as clusters of smaller silver nanoparticles

aggregate to form larger nanoparticles [8].

Sodium citrate in particular offers a simple and well characterized reaction.

Another common reducing agent, sodium borohydride, offers a more vigorous, rapid

reaction [26]. This is evident in comparison of the reduction potentials; sodium citrate's

reduction potential is -0.180V whereas sodium borohydride has a value of -0.481V [8]. In

recent years, efforts have been made to produce monodisperse silver nanoparticles from

so called "green" methods of synthesis. Gum acacia, or gum arabic, and

polyvinylpyrrolidone (PVP), among other plant-based resins, polymers, sugars, and weak

acids, have been used as capping and reducing agents [8, 27].

The reaction of silver nitrate with sodium borohydride produces a robust reaction [28]. Silver nanoparticles made with this strong reducing agent may be too small or too large for application within Raman spectroscopy, as lowered control over size comes with the rapid reaction time [28].

Photochemical reduction has been used to produce nanoparticles, one such synthesis with literature values of diameter in the 10-20nm range, controlled by PVP [8]. A laser pointed at a silver surface produces nanoparticles by laser ablation, irradiating a surface with energy until silver atoms and plasma particles are released which then aggregate to form solid particles [8]. This process begins with nucleation, followed by a phase transition, and finally the aggregation stage similar to what is seen in electrochemical reduction [8]. PVP was used to collect released silver shortly after it was emitted to prevent further aggregation, blocking the silver from forming larger nanoparticles greater than 50nm in diameter [8, 29]. The laser source typically makes this synthesis route an expensive choice [29]

The reduction with a solution of PVP containing solution and UV laser offers added long term stability to the final product by way of the hydroxyl groups of PVP forming coordination bonds with the nanoparticle surface, shown by Fourier-Transform Infrared Spectroscopy (FTIR) [8]. A pulsed sonoelectrochemical method utilized intervals of ultrasonic waves with stabilizer in solution to produce silver nanoparticles of 20-25nm. This method relies upon "massive nucleation" of silver [8]. Microscale bubbles in the solvent assist growth [8].

Chapter 3: Methods of Characterization

3.1: Theory of Ultraviolet-Visible Light Spectroscopy

Ultraviolet-visible spectrophotometry (spectroscopy) is an analytic technique in which the absorption and scattering of a sample may be used to determine concentration [7]. Light with a broad spectrum of wavelengths (200-800nm) is emitted by a laser [7]. This incident beam contacts the sample and is absorbed, scattered, or transmitted [7, 30]. Absorption of light wavelengths corresponds to movement of electrons in the valence shell up or down between atomic or molecular orbitals, called an electronic transition [7]. Given the wavelengths of incident light, valuable information of the valence shell electrons may be attained [8]. Transmitted light hits a detector and intensities of a broad spectrum of wavelengths may be analyzed. The intensity and location of a peak may be used to determine the chemical constituents of a sample [7]. This is because select transition metals exhibit color characteristics reflective of physical properties [7].

The ratio of emitted to transmitted light intensities is used to find absorbance in Equation 9, Beer's Law,

$$Absorbance = -log_{10}\left(\frac{I}{I_0}\right) = Concentration \cdot \varepsilon \cdot l$$

<div align="center">Equation 9: Beer Lambert Law</div>

The intensity of transmitted light is given by I, while incident light by I_o. The path length is l and wavelength-dependent absorptivity coefficient ε. Light not transmitted to the detector reflects upon the molar extinction. This quantity is proportional to both concentration and absorbance and scattering cross sections of the molecule(s) [7].

3.2: Theory of Dynamic Light Scattering

Dynamic light scattering is a technique which determines particle size by measuring movement due to Brownian motion [21, 31]. Particle velocity is found by analyzing the difference in diffraction patterns of a particle- containing solution; as a particle travels due to Brownian motion the frequency of light experiences a Doppler shift, or change, depending upon its direction toward or away from the source [21]. An algorithm may be used to first find a diffusion coefficient for the particles, and then to determine a range of particle velocities from the change in frequency. From the velocities, a distribution of masses may be found, as rate of movement due to Brownian motion can be related to mass [31]. Particles of greater mass are assumed to travel shorter distances, and particle diameter is directly proportional to mass, making calculation of diameters possible [31].

Surface structure and geometry may affect particle movement through the solvent [31], so the synthesized silver nanoparticles were assumed to be spherical as outlined in the literature and shown in TEM images. DLS data is limited by the polydispersity of the sample; if the sample contains particles with a wide range of particle diameters, the accuracy of DLS data declines [31]. Also of note is that the concentration of silver nanoparticles is important for DLS measurements; diluting too much would result in poor results. Statistically, increasing the sample size of particles, or using samples of higher concentrations, provided the sample is within a tolerable polydispersity, the better quality of data is acquired.

$$D = \frac{\Gamma}{\left(\frac{4 \cdot \pi \cdot n_o}{\lambda_o} \cdot \sin\left(\frac{\theta}{2}\right)\right)^2}$$

<div align="center">Equation 10: Correlation Relationship</div>

The software analyzes multiple correlation functions utilizing the decay rate (Γ), the

angle of scattered light (θ), the vacuum wavelength of incident light (λ_o), and the

refractive index of solvent (n_o), and then calculates a diffusion coefficient (D), shown in

Equation 10. Given the Stokes-Einstein, the temperature (T), solvent dynamic viscosity

(η), and diffusion constant (D) may be used to find the hydraulic radius of particles, (r_h).

$$r_h = \frac{k \cdot T}{6 \cdot \pi \cdot \eta \cdot D}$$

<div align="center">Equation 11: Stokes-Einstein Relationship</div>

3.3: Theory of Transmission Electron Microscopy

Transmission electron microscopy (TEM) is a technique used to image thin

<100nm samples at high resolution, capable of resolving objects to approximately 0.2 nm

[32]. Near the top of the TEM instrument is a thermionic gun, which is made of tungsten

wire that thins out, allowing electrons to be stripped off by a cathode [32, 33]. The

electrons are then accelerated toward a sample by a series of cathode and anode

electromagnetic focusing lenses [32, 33].

The denser a sample is, the darker it will appear, as electrons are not as capable of

passing freely though such a sample [32]. Samples must be dilute enough to allow for

the passage of some electrons. Electrons that do pass through the sample strike

scintillation coating and produce light due to the photoelectric effect [32]. From the

amount of electrons striking various regions of the scintillation coating, an image is

formed, reflecting the density and structure of the sample [32]. Increasing acceleration

potential of electrons used in imaging can afford improved penetration at the cost of

potential sample damage [32]. Signal convolution due to the electrostatic charge on the nanoparticles was expected, but believed to be minimal [32].

The appearance of sintering, or in-contact particle overlap, in a couple TEM images made analyzing particle size distribution difficult, likely introducing further error.

3.4 Theory of Zeta Potential

The zeta potential is a measure of electrostatic stability, and measures the repulsive and attractive forces between charged particles in solution [21, 22]. Surrounding a conventionally stable silver nanoparticle in solution is an electrostatic double layer, consisting of electrostatically negative ions such as citrate or borohydride. A Zetasizer measures zeta potential through determination of electrophoretic mobility using a Doppler determination of particle velocity with an applied electric field, once again measuring movement of particles through patterns of light scattering [22].

3.5 Theory of Scanning Electron Microscopy

Scanning Electron Microscopy (SEM) is a technique for imaging the surface topography, typically of a conducting material, with high resolution [32]. A tungsten wire thins out to a point and is heated; electrons are pulled off by a nearby anode [32]. Alternating anode and cathode magnetic coils produce the charge to accelerate the electrons along the desired path, focusing electrons to the sample [32]. These electrons bombard a sample and are deflected [32]. The electrons then contact detectors [32]. From the trajectory, the topology may be constructed [32]. The electron beam setup moves along the sample, moving in a pattern along the x and y coordinates [32]. The maximum image resolution is around 1nm due to limitations on the path of the electrons, as

electrons scatter [32]. Electrons do not follow perfectly linear and elastic paths, as they are charged particles. Theoretically the resolution is limited by the de Broglie wavelength, as the distance between two points must be greater than the wavelength of the emitted electrons for objects to be distinguishable [32]. As wavelength is inversely proportional to momentum, increasing the velocity of electrons striking the sample increases image resolution [32]. Achieving this is done by raising the acceleration voltage, but is theoretically limited by either the allowable voltage due to sample damage or maximum voltage of the machine [32].

Secondary electrons, or electrons emitted from the atom upon the arrival of an incident electron from the SEM [32], were the primary electrons used to form the images of CNF and silver substrates shown. These electrons exhibit inelastic scattering, as they are ejected from atoms following the entrance of the incident electrons [32]. Surface topology is visualized with these electrons [32]. Backscattered electrons are scattered off of sample nuclei, and are easiest to produce with samples of high atomic density [32]. These electrons indicate material differences; more specifically areas varying in atomic number will produce different shades in the image [32].

The detector is made of a Faraday cage, scintillation coating, and photomultiplier tube [32]. As electrons contact a scintillation coating, light is emitted [32]. The light then is directed to a photomultiplier tube [32]. As it strikes a dynode within the tube, electrons are released, moving to the next dynode [32]. The emission of electrons upon light's contact with certain metals is called the photoelectric effect [32]. At each subsequent dynode, the number of electrons is multiplied until they reach the anode, where the

current is measured [32]. Thus electrons fired from the thermionic gun are translated to photons, then back to electrons, and lastly to a current [32].

Difficulty arose when imaging samples of CNF substrate. As CNF is non-conducting, charge built up on the surface. Low levels of conductive silver nanoparticles did not allow for enough movement of charge off the surface. In order to take SEM images of the first sample made (2 CNF 3wt% : 1 AgNP) a common technique known as gold sputtering was utilized [34]. A minute quantity of gold was deposited into the sample, increasing conductivity. A metal box containing osmium tetraoxide, a vapor treatment, was also used, also to allow for greater sample conductivity [34]. Higher levels of silver nanoparticles in a second sample (2 AgNP : 1 CNF 3wt%) reduced the need for the imaging enhancement techniques.

Chapter 4: Experimental Procedures

4.1: Sodium Citrate as Reducing Agent for Silver Nanoparticle Synthesis

Sodium citrate is well characterized as a reducing agent, perhaps being the most common choice for synthesis of silver nanoparticles by reduction of silver salts such as silver nitrate [26]. It is a stronger reducing agent than ascorbic acid and as such is expected to produce a more monodisperse product [8]. It is also rather labile and does not sterically inhibit access to nanoparticles as a polymer might, important for SERS enhancement [27]. The 'other' product of this synthesis, sodium nitrate, will not negatively affect the reaction until at higher sodium citrate concentrations >10 mM the sodium ion will present a screening, or shielding effect discussed in the Background section entitled "Colloidal Stability."
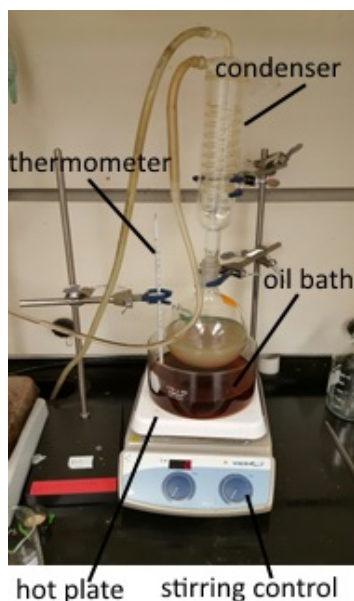
Figure 5: Experimental Setup

4.1.1: Experimental Setup

The experimental setup, shown in Figure 3, features a round bottom flask submerged in oil on a hot plate. A condenser situated above the round bottom flask reduces solvent loss from evaporation, keeping concentration of reactants fairly constant. A thermometer submerged in the oil bath was used to adjust and record temperatures. The motion of a stir bar within the round bottom flask is controlled by a magnetic hot plate. Both the revolutions per minute of the stir bar and temperature are adjustable. The stir bar was set to a high rate of stirring as

a greater convection current was proposed to produce a more controlled reaction rate. Early synthesis used water from a sink that may have contained chlorine or chemicals which would affect the reduction or nanoparticle growth chemistry. For this reason, deoxygenized, deionized water from a 17Ω Milli-Q Water Purification System was used for synthesis until the instrument was damaged. For all data using the reduction by sodium citrate only within this paper, deionized water not from the Milli-Q system was used. A 500 mL round bottom flask was used for synthesis of silver nanoparticles with citrate as reducing agent except for the synthesis of the 1:10 ratio which produced silver nanoparticles imaged by TEM and ~5 nm diameters according to DLS measurement. Samples of the synthesis products were taken with a Pipetman, after temporary removal of the condenser for synthesis with the RBF without multiple necks.

4.1.2: Reduction of Silver Nitrate by Sodium Citrate

The following procedure has been adapted from procedures in *Synthesis of Monodisperse, Quasi-Spherical Silver Nanoparticles with Sizes Defined by the Nature of Silver Precursors* [26]. Table 1 gives the amounts of chemicals used in this synthesis.

Table 1: Chemicals Involved in Silver Nanoparticle Synthesis with Sodium Citrate Reducing Agent

Chemical	Material Type	Amount [mMl]	Converted amount
Silver Nitrate	Solid, Powder	1	0.034 grams
Trisodium Citrate Dihydrate	Solid, Powder	between 5 and 10	0.294 to 0.588 grams
Water	Liquid	N/A	200 mL

Prior to beginning the experiment, the hot plate was turned on and temperature increased to 170˚C. The procedure began with sonication of both silver nitrate and sodium citrate solutions for 5 minutes. Sonication increases homogeneity within the

solutions, as the crystal lattice structure of reactants is broken up by the sonic waves and dispersed [27]. Bulk molecules within a crystal are not able to react with silver nitrate; sonication frees trapped bulk molecules, increasing the reaction's surface area to volume ratio [27]. This process was tested to increase reproducibility of reaction rate. Under a specific set of conditions such as with certain organic solvents, sonication of silver nitrate may also give rise to silver nanoparticles; the silver molecules bombard one another in the sonicator. Sonication time should be limited despite the aggregation likely to occur being negligible as compared to later chemical reduction and subsequent nucleation [8, 27].

The stirring was set at a highest attainable rpm for which the stir bar maintained constant stirring (position 5 out of 6). Once the oil bath had reached approximately 99˚C, the 150 mL sodium citrate solution was added to the round bottom flask, and the temperature of the hotplate was adjusted as necessary to maintain 99˚C for 30 minutes. Upon addition of the silver nitrate the temperature decreased to approximately 95 ˚C, and needed to be increased to reach 99˚C. Adjustment of the hot plate to 180 ˚C hastened the process of the added solution approaching a thermal equilibrium at 99˚C. This temperature is maintained for 35 minutes, until an opaque green color is attained

Figure 6: 500mL Silver Nanoparticle Solution Reduced by 10mM Citrate

for all citrate ratios from 1:7 to 1:10. Due to problems in reproducibility, sometimes the reaction was stopped not at 35 minutes but at a time between 30-45 minutes; color was believed to be a better indicator of when the reaction was completed. Reflux conditions were avoided, as less control over size range results from solution temperatures greater

than 100˚C [26, 27]. For TEM imaging, UV-Vis, and DLS, the reaction was stopped at 35 minutes for each ratio of silver to citrate synthesis by removal from the oil bath. In other synthesis, samples were taken at 5 minute intervals once color appeared, typically starting around 30 minutes into the reaction.

4.1.3: Observation of Citrate Controlled Silver NP Synthesis

Visual colorimetric comparison suggests that nanoparticles synthesized by 1:9 or 1:10 silver: citrate ratios have the potential to produce reasonably monodisperse nanoparticles within the desired size range, whereas 1:5 and 1:6 ratios produce broad size ranges. The 1:20 ratio rapidly produced large clustered aggregates >100 nm. A nanoparticle solution with a green color, as in Figure 6 in the top third of the vial, is a good example of silver nanoparticle solution likely within the desired range, which would be tested to confirm this with UV-Vis and DLS data. Closer to the bottom of the vial in Figure 6, the color transitions to tan and then darker brown or grey, which indicates that there are larger or aggregated nanoparticles present.

4.2: Tannic Acid as Reducing Agent for Silver Nanoparticle Synthesis

Tannic acid lowers pH in addition to acting as a weak reducing agent [25]. Both tannic acid and sodium citrate will reduce silver, at unique rates [25, 35]. In lowering pH, tannic acid may affect the colloidal system's pH. As a result it may alter the nanoparticle's surface and its protective electrostatic double layer [21]. Consequently the likelihood of citrate both reducing silver and silver nanoparticles colliding to form an aggregate may be negatively affected [21]. At low pH the solution lacks free electrons as citrate's hydroxyl groups will be protonated, and lack the negativity utilized for both

reduction and repulsion when citrate ion is adsorbed to the nanoparticle surface. The full effects of pH upon the reaction may not fully be understood, but it was considered to affect the length of the stages of nanoparticle growth including nucleation, coarsening, and aggregation [25].

Tali Dadosh was successful in achieving control of particles from diameters of 18-30nm with standard deviations below 15%, and found that a plot of log tannic acid concentration against silver nanoparticle diameter resulted in a linear fit [35] Larger nanoparticles synthesized via tannic acid and citrate reduction of silver nitrate exhibited less spherical geometries, and thus higher aspect ratios [35].

4.2.1: Experimental Setup

The experimental setup used for the recipe with tannic acid and sodium citrate as reducing agents was adjusted from that used in reduction with sodium citrate alone. The same oil bath, hot plate, and thermometer setup that can be seen in Figure 5 was again used to control reaction temperature. The sonicator was not used during these experiments, and a three pronged, 500mL round bottom flask was used as a reaction vessel with the condenser in place. The two prongs on either side were capped with rubber stoppers which were removed for sampling. This sampling was taken with a Pipetman. Milli-Q deionized, deoxygenated water was used for experimentation with tannic acid as reducing agent. Stirring was not as optimal during this synthesis, and was set at position 4 out of 6. Sampling did not require the removal of the condenser, as a rubber stopper was removed from one of the side necks of the RBF for a pipette to be lowered into the RBF.

4.2.2: Silver Nanoparticle Synthesis by Tannic Acid

The following procedure was adapted from *Synthesis of uniform silver nanoparticles with a controllable size* and *Synthesis of Highly Monodisperse Citrate-Stabilized Silver Nanoparticles of up to 200 nm: Kinetic Control and Catalytic Properties* [35, 25].

Table 2: Chemicals Involved in Tannic Acid and Sodium Citrate Reduced Nanoparticle Synthesis

Chemical	Material Type	Amount	Converted amount
Silver Nitrate	Solid, Powder	3.34 mM	0.085 grams
Trisodium Citrate Dihydrate	Solid, Powder	2.95 mM	0.13 grams
Tannic Acid	Solid, Powder	0.66 mM	0.17 grams
Water	Liquid	N/A	150 mL

Table 2 gives the amounts of chemicals used in the synthesis using tannic acid and sodium citrate. The experiment starts with 100 mL of reducing agent solution stirring with the hot plate set to 180°C. The speed of the stirring was set to position 4, and was constant throughout the reaction. The reducing agent solution was allowed to stir on the hot plate for approximately 30 minutes, which brought the solution to the desired temperature and assisted in dissolving the reducing agent. Once the reducing agent solution had completely dissolved and reached the appropriate temperature of about 95°C, 50 mL of solution containing silver nitrate at 10 mM was quickly added to the reaction solution. The reaction was left to sit while stirring for 45 minutes, while samples are taken about every 10 minutes. The concentration of silver nitrate upon addition to the RBF was found to be approximately 3.34 mM. After 40 minutes was reached the reaction was cooled to room temperature and observation of a golden, amber, or brown hue followed depending upon reducing agent concentration and reducing strength.

4.2.3: Size Exclusion by Filtering

A syringe filter was tested for separation of different silver nanoparticle size

ranges. The silver NP solution tested for the syringe filter's efficacy was taken from a

polydisperse silver sol synthesized via silver nitrate reduced by tannic acid and sodium

citrate. A 100 nm syringe was used first, followed by a 20 nm filter. The syringe is first

filled with the solution of silver nanoparticles, and then the filter inserted onto the

syringe. The plunger was removed, or pulled upon until the parts separate. The plunger

was then inserted and inverted, as pressure slowly applied. The unwanted nanoparticle

precipitate of the first filtering was trapped in the syringe, while nanoparticles <100 nm

were not excluded by the filter, and were expelled in solution into a glass beaker. The

process was repeated with the 20 nm syringe filter, this time the expelled solution was not

desired. The remaining nanoparticles were rinsed from the filter using deionized water in

a squeeze bottle into a beaker. Due to the fragility of the syringe filters, it was imperative

that pressure be applied slowly to avoid damage and preserve the integrity of the filter's

size exclusion.

4.2.4: Application of Centrifugation

Centrifugation procedure was adapted from *Fast and cost-effective purification of gold*

nanoparticles in the 20-250 nm size range by continuous density gradient centrifugation

[36]. Centrifugation is a common technique to separate materials of unequal mass and

consequently size in a liquid suspension [21]. The theory of sedimentation dictates the

behavior of a vial's contents upon centrifugation. Centripetal forces, or gravitational

force in sedimentation, oppose viscous and buoyant forces as particles are forced to the

bottom of the vial [21]. The centrifuge expedites the same process of sedimentation by

application of the relative centrifugation force, or RCF. This force is a function of both

$$RCF = 1.1118 \times 10^{-5} \cdot Radius(cm) \cdot Speed(rpm)^2$$

radial distance and angular velocity of the rotor as Equation 12 shows, and can vary from instrument to instrument. Sample tubes are held in the metal slots of the centrifuge at an angle and accelerated up to over 150,000 rpm, generating forces 1 million times that of gravity. A speed of 12,000 rpm was used for separation of silver nanoparticles taken from a polydisperse silver sol with tannic acid and sodium citrate as reducing agents.

4.3: Gum Arabic (Acacia) as Reducing Agent for Silver Nanoparticle Synthesis

Gum arabic may act primarily as a capping agent, but also has been indicated to be a weak reducing agent [27]. The hydrophobicity of gum arabic was proposed to be beneficial, as hydrophobic contaminants may be more easily concentrated when in contact with gum arabic reduced silver applied locally to the substrate. However, this method was not optimized for reproducibility. Synthesis with gum arabic first began without added sodium citrate, and was a long process. The resulting silver nanoparticles appeared to be undesirably small, approximately 10 nm. Sodium citrate was added to both increase the reaction rate and ensure synthesis by chemical reduction rather than thermal decomposition was occurring.

4.3.1: Experimental Setup

The experimental setup used for the recipe with gum arabic and sodium citrate as reducing agents was the similar to that for reduction by tannic acid and sodium citrate. The oil bath was used to heat the 3 pronged RBF containing solution, with condenser attached.

It was noted that the hydrophobic nature of gum arabic may have caused some difficulties in ensuring that all reactant was properly transferred into the RBF. Gum arabic powder was seen adsorbed to the glass beaker after transfer of reducing agent solution. The Erlenmeyer flask in which gum arabic was added to water was swirled for approximately 60 seconds and sonicated for 30 minutes in hopes that better dispersion would be achieved. The Erlenmeyer flask, funnel, and RBF neck were inspected for gum arabic to determine if transfer was successful.

4.3.2: Silver Nanoparticle Synthesis by Gum Arabic

The following procedure has been adapted from *Facile and one-step synthesis of monodisperse silver nanoparticles using gum acacia in aqueous solution* [27]. Amounts of chemicals used in this process are outlined in Table 3. The gum arabic was carefully added to 70 mL of dIdO water, followed by sodium citrate. The sodium citrate was not in molar excess of silver nitrate, and is unlikely to reduce all silver itself (one citrate ion may be capable of reducing multiple silver ions [26]). Sonication for 30 minutes was done to reach greatest homogeneity and best transfer of reactants. This reducing agent solution was added to a 3 pronged 500mL RBF. After approximately 30 minutes or when the reaction temperature reached 99°C, the silver nitrate solution was added. Silver nitrate was at a significantly higher concentration in this synthesis than in other methods used, which could have resulted in the wider size distribution indicated by UV-Vis and DLS data.

Table 3: Chemicals Involved in Gum Arabic and Sodium Citrate Reduced Nanoparticle Synthesis

Chemical	Material Type	Amount	Converted amount
Silver Nitrate	Solid, Powder	0.2 wt%, 9.9 mM	0.2 g
Trisodium Citrate Dihydrate	Solid, Powder	0.5 mM	0.018 g
Gum Arabic	Solid, Powder	0.3 wt%	0.35 g
Water	Liquid	N/A	120 mL

4.4: Sodium Borohydride as Reducing Agent for Silver Nanoparticle Synthesis

Borohydride was the most vigorous reducing agent used. As a strong reducing agent, the reaction proceeded most rapidly, and small nanoparticles of about 10 nm in diameter were synthesized. If allowed to continue, these 10 nm particles were found to aggregate to particles of 100 nm or greater. The borohydride ion, like the citrate ion, may form an electrostatic layer covering the silver nanoparticles produced. Once again, this increases the colloidal stability.

4.4.1: Experimental Setup

A 200 mL Erlenmeyer flask was used as a reaction vessel for reduction by sodium borohydride. The hot plate was used only for its stirring function, which was kept at position 4. The Erlenmeyer flask was placed on an ice bath measured to be about 0°C. This synthesis lacked a condenser, as temperature was lowered from room temperature at 23°C.

4.4.2: Silver Nanoparticle Synthesis by Sodium Borohydride

Procedure was adapted from *Synthesis and Study of Silver Nanoparticles* [28]. Table 4 outlines the quantity of reactants. The solution of reducing agents was chilled to about 0°C in a 200 mL Erlenmeyer flask placed on an ice bath. The temperature deviation

Table 4: Chemicals Involved in Sodium Borohydride Reduced Nanoparticle Synthesis

Chemical	Material Type	Amount	Converted amount
Silver Nitrate	Solid, Powder	0.16 mM	.0011 g
Sodium Borohydride	Solid, Powder	1.5 mM	.0023 g
Water	Liquid	N/A	40 mL

from a literature value of 60°C was designed to gain more control over size by reducing the energy of the reaction and consequently reaction rate. The silver nitrate solution was added dropwise at about 1 drop per second and stirred for 20 minutes or until an intense yellow color appeared.

4.5: Cleaning

Nitric acid, 5M, was used to clean glassware in contact with silver. As a strong base, the nitric acid reduced any silver in solution and overcame the surface energy of nanoparticles to degrade them. To ensure that the nitric acid and silver was removed from glassware, it was rinsed 25 times with water.

4.6: Raman Spectra of Crystal Violet

Spectra of dilute crystal violet solutions at 8.29 μM were taken after the solutions were added to both silver-CNF and silver-CNC composite matrices. The CNF and CNC composite matrices were prepared under similar conditions, beginning at 2wt% or ~98% (the expansion of water into ice affects porosity so the actual porosity should be slightly greater than 98%.) 50 mL 3wt% CNF slurry was mixed by hand with 100 mL of the 1:10 citrate reduced silver nanoparticle solution. To also reach 2wt%, 50 mL CNC was mixed by hand with 133 mL silver nanoparticle solution produced with the 1:10 Ag : Citrate ratio described in the experimental section. These samples were frozen in a -82°C freezer. Raman shift, or wavenumber, was recorded using an ACTON SpectraPro2300i at 532 nm laser light and varying power.

4.7: Porosity

Figure 7: Removing CNF (no Silver NP) Sample from Drying Setup

Figure 8: CNF Sample (no Silver NP) after Removal from Drying Setup

Figure 9: CNF Sample (no Silver NP) after Removal from Freeze Dryer

To correlate porosity of CNF composite matrices with time, 10 L of CNF slurry at 3wt% produced from the University of Maine pilot plant was mixed with 5 L water dried in a setup shown above made on all sides of porous stone bricks. Sampling began 45 minutes after adding the slurry of CNF and water (or CNF and silver nanoparticle solution) into the drying setup. Samples were taken at varying intervals that provided a range of porosities. For the first 2 hours, samples were taken about every 30 minutes. The next 6 hours samples were taken hourly. Sampling intervals increased to 90 minutes, 3 hours, 4 hours, 6 hours, 12 hours, and 24 hours.

At each sampling time, 6 samples were taken; 3 for porosity experiments and 2 for Raman spectra background, with one spare. Early sampling procedure was to scoop up the pudding-like CNF with a knife and tap the box to make a flat surface filled up to a line on the plastic boxes, making a 2 mm thick sample. Later thin square samples were retrieved or sliced with a knife from the CNF drying setup's bulk at a depth of roughly 4 inches, pictured in Figure 7. Once the CNF had dried to the point of characterization as a mushy, cakelike substance, blocks of the drying setup were removed, and a large cube of CNF sample cut out. From this larger cube, the sides were removed by a knife, and 2 mm thick squares that fit into the plastic boxes were taken. The sides were cut off to ensure samples tested for porosity contained no dust or irregular pore sizes that may be found in the skin, or outer layers. Great care was taken not to touch sample and or apply pressure. Samples in their plastic boxes were wrapped carefully in Parafilm. The Parafilm was necessary to make an air tight barrier so little drying occurred after removal from the drying setup. It was necessary as access to liquid nitrogen and the -82°C freezer could not be guaranteed. The samples were later dipped in liquid nitrogen to rapidly freeze water still contained within the CNF, locking in the porous structure. This was followed by storage in the -82°C freezer.

A proprietary method for determining the porosity of CNF substrates was used upon the suggestion of Professor Douglas Bousfield. The porosity was back-calculated starting with the mass of samples after removal from the freezer. Next the volume of total occupied space, the sum of void and CNF volume, was found. This was done by applying Avogadro's principle of water displacement. The proprietary procedure developed was to submerge the composite matrix samples in silicone oil overnight, and find volume of

silicone oil occupying pores through displacement of water. Silicone oil was chosen for its ability to diffuse into the pores without altering the 3D structure and thus conserving porosity. Silicone oil's viscosity, 5 poise, resulted in its retention within the samples during porosity measurements. Samples were submerged in ice cube trays filled with silicone oil and allowed to sit overnight, or over 12 hours. Larger pores appeared to fill within a matter of hours whereas samples were left overnight so that smaller pores would be filled by capillary action. For lower porosity samples which are held within the drying setup longer, the pore sizes are smaller. This is responsible for error, as silicone oil is less likely to completely fill smaller pores. Excess silicone oil on the surface of the aerogels was carefully removed with Kimwipes.

The mass of samples are taken after removal from the freezer, and then again after being submerged in silicone oil overnight. This was used to find the mass and then volume of silicone oil filling the pores $V_{Si\,oil}$, using silicone oil's density. The volume of water displaced upon submerging samples saturated with silicone was recorded and used as the total volume of samples, $V_{CNF}+V_W$. The porosity is then given by Equation 13,

$$Porosity, \varphi = 100 - vol\%\,water = 100 - \frac{v_{Si\,oil}}{v_{CNF} + v_w}\,X\,100$$

Equation 13: Porosity Relationship

There currently appears to be no literature values for the drying of CNF to correlate time and porosity under similar conditions. We understand there will be deviation from the real value of porosity due in large part to the inability of silicone oil to gain access to smaller pore sizes. To a lesser extent the value will also accrue error from the expansion of pores after application of liquid nitrogen and drying that occurs from the air trapped in the plastic boxes. The volume of plastic boxes is constant and sample

volumes assumed to be of small volume for which the effects of this drying would remain constant throughout all samples, as the volume of air trapped would be constant.

4.7.1: Application of Liquid Nitrogen

Liquid nitrogen is used to "lock in" the 3D structure of CNF of certain porosity. This is intended to prevent alteration in the 3D pore structure of micro-capillaries within the CNF after varying drying times. Samples within their plastic boxes are placed in glass containers, which are each sealed with Parafilm and placed in a Styrofoam box within a hood. Liquid nitrogen is poured into the Styrofoam box, rapidly freezing water contained within samples, or so-called ice templating.

4.7.2: Lyophilization

During lyophilization, or freeze drying, water is removed from a sample [37]. This occurs through sublimation. Depending upon the samples, this may lower stability [37]. The water within samples is frozen in liquid nitrogen prior to being inserted into the freeze dryer at -82°C. The vacuum of the freeze dryer has a maximum capacity of approximately 12 mT, but ran as high as 36 mT. As pressure is decreased, water sublimates, which ideally results in a stable, compact composite matrix with better

Figure 10: CNF Samples of Varying Porosity with Applied Vacuum on the Freeze Dryer

long-term invariability [37]. During lyophilization the composite matrices may be subjected to a wide range of pressures.

4.8: pH Control

The pH of nanoparticles synthesized via the 1:10 ratio of citrate reducing agent was adjusted by two methods. Muhammad was successful in adjustment by dropwise addition of 1M sodium hydroxide, shown in Figure 12. This early experiment showed neutral to basic pH values as having the greatest stability. Zeta potentials were maximized as slightly basic pH values, and nanoparticles did not visibly fall out of solution.
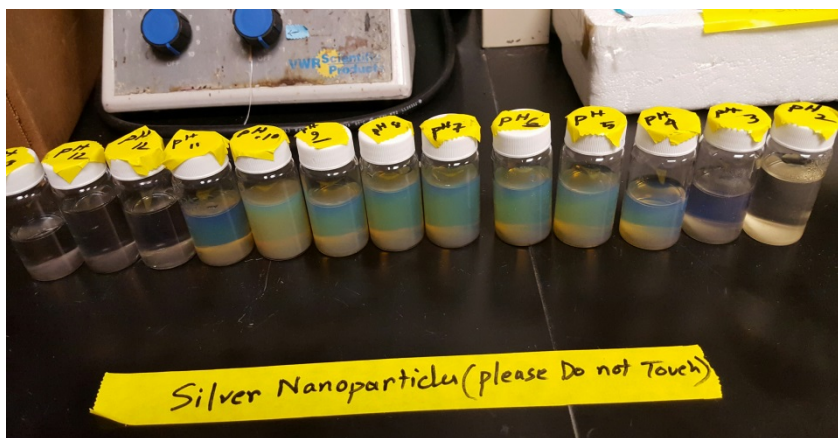
Figure 11: Silver Nanoparticles Solutions of varying pH. From Left to Right: pH 14 – pH 2

As the sodium hydroxide was a strong base, it was determined the experiment should be tested with both sodium citrate to maintain an unaltered system, as well as a separate experiment with a weaker base in sodium bicarbonate.

For pH control with sodium citrate, varying small amounts of sodium citrate powder were added to 20mL of the same silver nanoparticle solution. This solution was sonicated for approximately 60 seconds to obtain a homogenous solution and pH measured by a Thermo Orion 3 Star pH Benchtop instrument shown in Figure 13. After pH was recorded, the silver solution was pipetted into a zeta cell and absorbance measured, followed by a measurement of zeta potential in the Malvern instrument.

Figure 12: Measuring pH of Silver
Nanoparticles Solutions

pH control by addition of sodium bicarbonate was done by dropwise addition of 1M sodium bicarbonate solution to 20 mL of silver NP solution. Rather than sonication, this solution was mixed by shaking for 20 seconds. Its pH, absorbance, and zeta potential were then measured as was done for pH control by sodium citrate.

Chapter 5: Results

5.1: General Observation and Remarks

Compared to gold nanoparticles, the size distribution of silver nanoparticles is typically much more difficult to control, making the term "monodisperse" relative. This project was marked by a pattern of minor early success followed by difficulty reproducing results. Synthesis with tannic acid and sodium citrate reduction of silver nitrate, for example, was successful in production of a remarkably monodisperse sample twice, but failed to produce this size distribution upon further synthesis attempts. Similarly synthesis by gum arabic was believed to show promising results, but synthesis was slow, and perhaps gum arabic being too weak a reducing agent to produce consistent results.

At times it would appear as though the 1:5 silver nitrate to sodium citrate ($AgNO_3$:NaCit, Ag:NaCit, Ag:Cit) ratio might produce a tighter distribution than mid-

range ratio synthesis, such as 1:7 or 1:8 $AgNO_3$:NaCit. By visual observation, this does not appear to be the case, as the 1:5 and 1:6 consistently produced tan solutions, indicative of a broad size range. Tan indicates absorption across a range of wavelengths, and UV-Vis spectra show a broad absorbance peak spanning this greater range. This may be explained by the relationship between nanoparticle size and absorbance peak, as a solution containing a broader range of nanoparticles will absorb light at intensities associated with each particle size. However, DLS at times pointed to 1:5 having better than expected distributions. Perhaps this is due to a bimodal distribution, with larger aggregated particle clusters in very small concentration and a second, tight peak of small nanoparticles. Comparatively, other ratios may show broader distributions, but lack the largest of micron scale aggregated clusters found in the 1:5 ratio's TEM images and at times in DLS data.

As a summary of what was found, it appeared that reactant solution at a ratio of approximately 1:10 $AgNO_3$:NaCit maximized the control over silver nanoparticles produced without interfering with long term stability and Raman spectra. Synthesis with both tannic acid and sodium citrate as reducing agents shows equal if not better sizing data, but may not be ideal for application in Raman spectroscopy. Its potential interference with data collection through scattering of light and other means are not well known. Tannic acid would likely easily be displaced to allow biomolecules access to silver nanoparticles for SERS enhancement, but this too has not been tested within a CNF composite matrix. Although it may take a great deal of time, it is believed the properly sized silver nanoparticles may be synthesized via sodium citrate at approximately 10 mM.

Samples chosen for discussion within this section were either further elucidated by TEM, or were picked because their size distribution best fit the target of monodisperse particles with 30-50 nm diameter, which are of interest for tests within CNF composite matrices for Raman spectroscopy. It is believed this size will allow for best surface coverage within the CNF matrix, and may be entrained by the fibers of CNF. The 1:20 ratio, for example, was not included as it showed no evidence of containing particles <100 nm.

5.2: Ultraviolet-Visible Light Spectroscopy Results

The following UV-visible light spectroscopy results were analyzed in the wavelength window from about 300 nm to 800 nm. This was due to an abundance of noisy absorbance data below 300 nm. For visual ease of comparison, the data for the wavelengths below 300 nm were omitted. The most useful UV-visible light spectroscopy data for silver nanoparticles typically lies between 350-550 nm, as this is where a characteristic peak lies that may give some information on particle size. All UV-Vis and DLS measurements were made with solution in disposable plastic cuvettes as water was always used as the solvent.

A number of colors were observed over the span of silver synthesis. Typically, reduction of silver nitrate by 10mM sodium citrate would result in color by 30 minutes, and reach a light green opaqueness by 35 minutes or dark green by 40 minutes. Reduction by 5mM sodium citrate appeared to produce a distinguishable color most rapidly, and to reach reaction completion before reduction by 10mM sodium citrate under similar conditions. However, synthesis with citrate at both 1:5 and 1:6 Ag:NaCit never produced the green color, but did produce tan sols. This may be considered indicative of a

heterodisperse particle solution, or large, undesired size ranges, as absorbance peaks for the tan sols show a broader range of wavelengths. Additionally, light is absorbed at longer wavelengths, which is once again typical of solutions with larger particles present.

Small nanoparticles <10 nm with tight size distributions often produced a light yellow hue. This was not seen in reactions using only sodium citrate as reducing agent in which all reactants were added at the beginning of synthesis, but was seen in reduction by sodium borohydride and with some of the samples for synthesis by gum arabic or by tannic acid. Reduction by tannic acid typically produced a solution of amber hue. It may be of importance to note that tannic acid is a brownish color itself.

Green silver sols are perhaps the most common. They may be described as containing a murky brown or grey tint to them if they are aggregated and of greater sizes and wider distributions. Green with hints of tan and yellow was most commonly seen; the 1:7-1:10 ratios with citrate could all be described as producing green sols with a tan tint. Grey or black color is typically only seen with aggregated solutions.
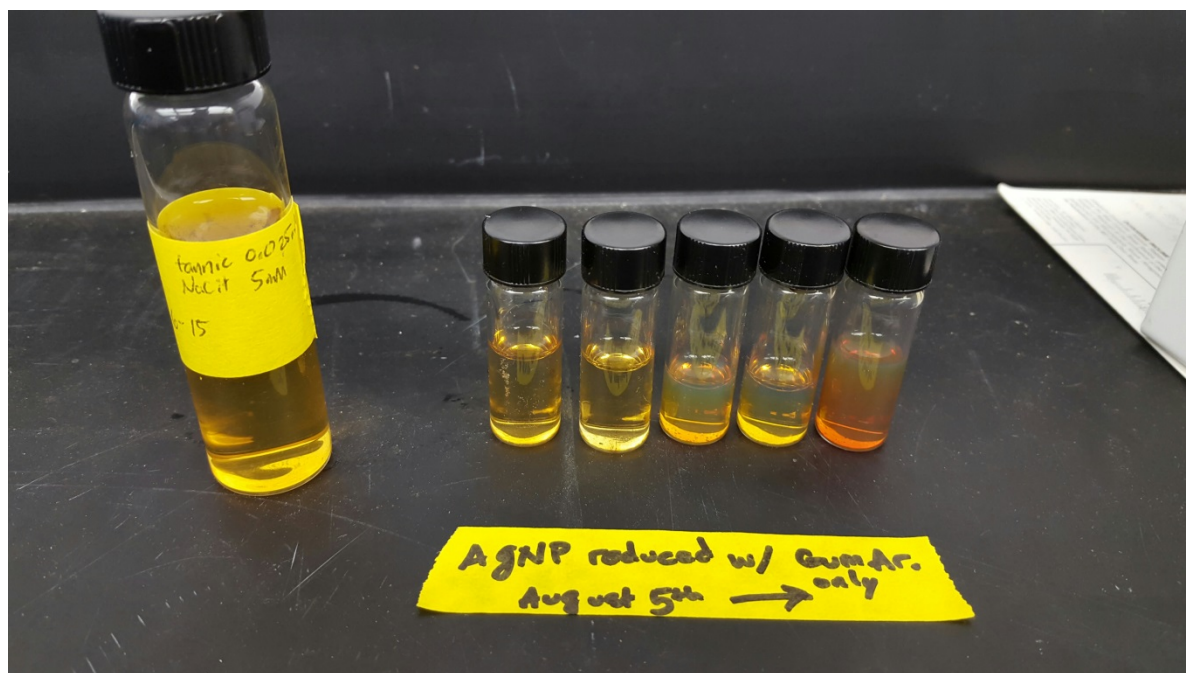
Figure 13 shows that silver nanoparticles solutions synthesized via silver nitrate reduced by tannic acid and sodium citrate is shown to be a dark yellow, at far left in the larger glass vial. To the right of this silver sol, the silver nanoparticle samples reduced with gum arabic are arranged from left to right with the longest synthesis duration on the far right, and first sample to the left. Darker amber is present in later samples, whereas early samples show a more translucent yellow hue.

5.2.1: Silver Nanoparticles: Co-Precipitation Method, 10mM Sodium Citrate

Figure 14 below shows the UV-Vis spectrum and thus absorbance pattern of the silver nanoparticles synthesized using 10 mM citrate reducing agent and 1 mM silver nitrate, in addition to a Mieplot simulation of absorbance spectra for 10 nm silver

particles dispersed in water. The process used to obtain this spectrum involved no

dilution of synthesis solution.
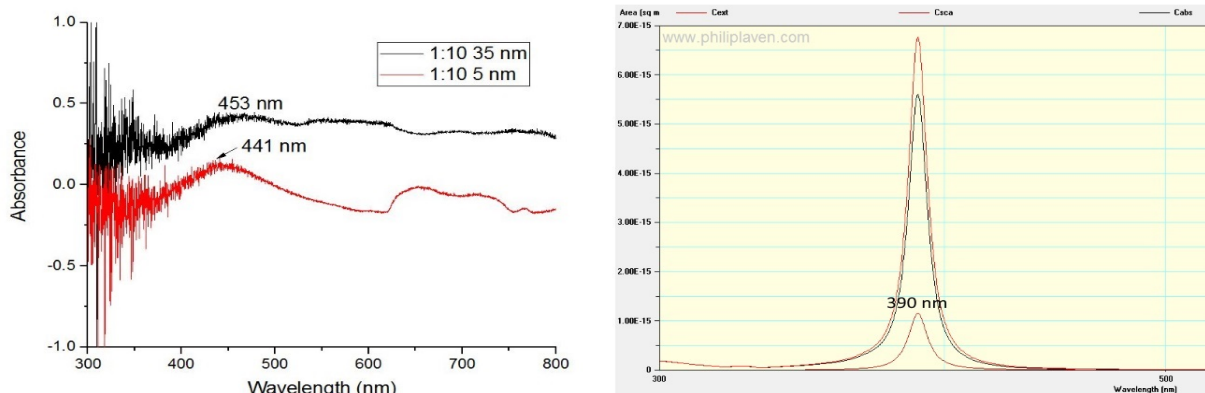
Figure 14: UV Vis of Silver Nanoparticles Synthesized by 1:10 Ag:Citrate on Two Different Occasions Compared to Simulation Left: Spectra of Two Synthesis of 1:10 Silver NP, Right: Mieplot Simulation of 10 nm Silver NP

The red spectrum with peak absorbance of approximately 441 nm from Figure 10 was

taken of the 1:10 Ag:NaCit synthesis that was sampled for TEM images shown later.

DLS number data discussed later pointed to this sample as being primarily small

nanoparticles approximately 5 nm in diameter, mostly all 10 nm or below. Its peak is

sharper than that of the 1:10 sample shown to contain larger particles. The peak around

650 nm could indicate larger particles, though one may consider it to be noise. The black

UV-Vis spectra shown in the graph at left in Figure 14 of the 1:10 silver to citrate

synthesis with DLS data showing the greatest number of particles having a diameter of

approximately 35 nm shows a secondary, minimally intense and broad peak around 550

nm. It is at this wavelength one might expect a secondary peak indicating the presence of

aggregated particles. Differences in synthesis may be primarily attributed to difficulty

reaching and maintaining a constant, desired temperature throughout synthesis, or due to

failure in timing of the reaction. Other potential causes of deviation in produced

nanoparticle sizes may be aggregation after synthesis and a decline in the quality of

chemical compounds used in synthesis over time. The round bottom flask volume also

changed, and thus stirring may have been greatly affected.

Both spectra taken experimentally show deviation from Mieplot simulations

assuming DLS measurements are accurate. The Mieplot peak for 10 nm particles is below

400 nm, while the spectra for 1:10 that produced smaller particles peaks past 440 nm.

Similar Mieplot spectra to those shown in Figure 14 for particles of 30 nm indicated

according to Mie theory a peak is predicted at about 420 nm. It was expected that the 10

mM citrate UV Vis spectra would have peaks at a wavelength of approximately 420 nm

or as low as 400 nm for 10 nm silver nanoparticles as seen in the literature chart from

Sigma Aldrich below in Figure 16, but the spectra obtained show a red-shifted product, as

seen in Figures 14 and 15. This may be due to synthesis of a heterodisperse sol; as stated

the black spectrum shows a second peak around 550 nm, which may indicate aggregated

particles were present. The synthesis which produced 10 nm particles peaks at

approximately 440 nm, whereas the synthesis which produced 35 nm particles at 450 nm.

This red-shift does support the existence of larger particles in the sample which gave the

black spectrum, perhaps with diameters of 35 nm or larger.
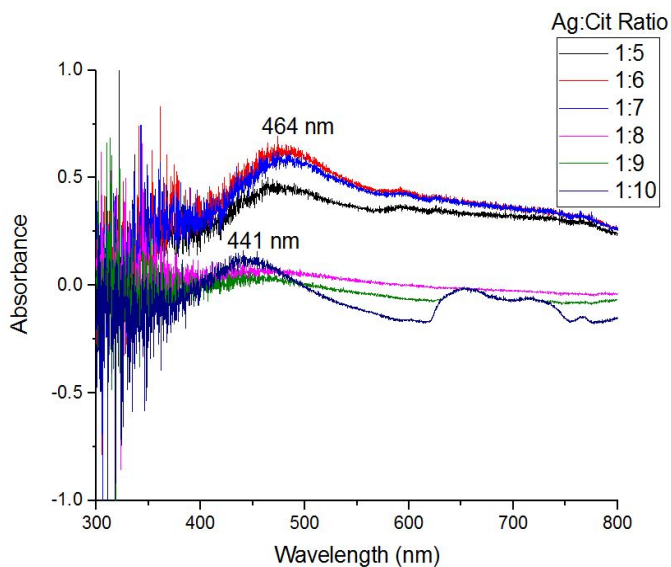
5.2.2: Comparison of UV Vis Spectra for Silver Nanoparticles Synthesized by Various Concentrations of Sodium Citrate to Literature Values

Figure 152: UV Vis Spectra Comparison between Initial Citrate Concentration
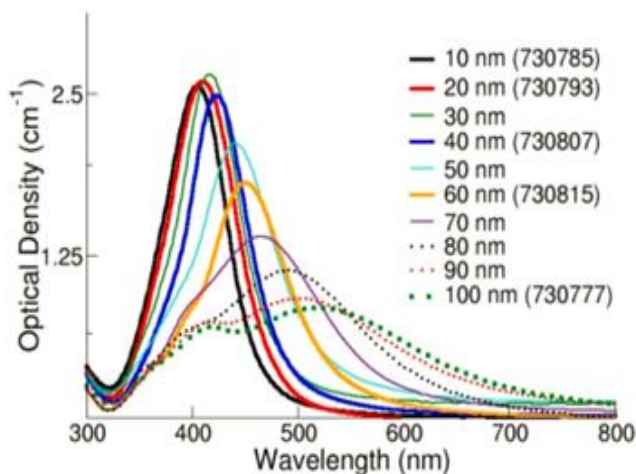
Figure 3: Literature UV Vis Spectra of Silver Nanoparticles of Varying Sizes from Literature Values, Sigma Aldrich [13]

Notably, the spectra obtained from Sigma Aldrich are measurements of optical density, which normalizes for path length in Beer's Law. From this literature, on may assume larger particles are red-shifted and produce broader peaks. Both 1:9 and 1:10 produced similar peaks, red-shifted from the expected literature values of <420 nm, instead having slightly broad peaks between 420-450 nm. The 1:8 ratio shows a broader peak, and likely was not a sol of ideal polydispersity or did contain aggregated nanoparticles. The UV Vis spectra of the 1:5, 1:6, and 1:7 ratios show a red-shift in comparison to higher citrate concentrations, with greater optical density due to the larger absorption cross section related to nanoparticle size. The data supports that these citrate concentrations contain larger particles than the 1:10 ratio. Spectra of these three ratios are of a similar shape, with a lower absorbance peak past 550 nm, indicative of some aggregation. At 35 minutes, the time the reaction was stopped for all ratios, silver nanoparticles from the 1:9 and 1:10 ratio appear to still be in an earlier stage of nucleation, whereas silver nanoparticles in ratios such as 1:5 are aggregating. A peak past 550 nm exhibited by 1:5, 1:6, and 1:7 ratios shows that these ratios contain aggregated nanoparticles, larger than desired ranges.

5.2.3: Silver Nanoparticles-Comparison between Reducing Agents

The following UV-Vis spectra were taken of samples from the synthesis of silver nanoparticles by various reducing agents. Due to the dependence of the plasmon resonance upon particle size, a general trend of larger particles having absorbance peaks at higher wavelengths may be seen. Following this trend, sodium borohydride produced the least red-shifted, and smallest, nanoparticles. The citrate ratios produced the longest wavelength absorbance peaks; for all citrate ratios it appears the produced nanoparticles are red-shifted in comparison to literature values. Perhaps this may be attributed to the dielectrics.
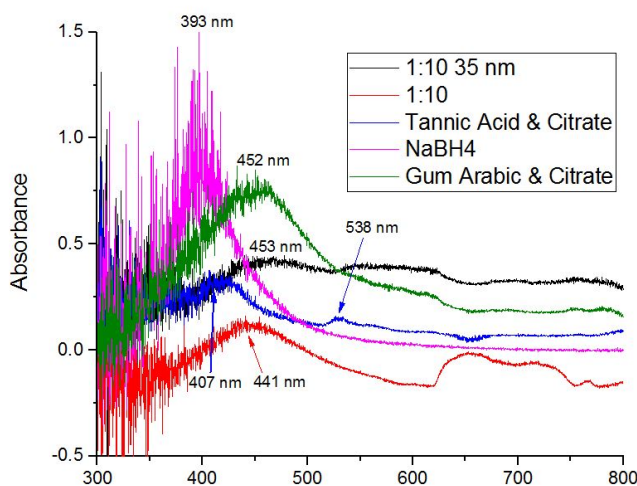
Figure 17: UV Vis Spectra Comparison of Silver Nanoparticles Synthesized with various Reducing Agents

Tannic acid produced a spectrum well in line with literature values, around 420 nm, which was later supported by a DLS number% peak between 30-40 nm. The 1:10 citrate ratio which was reported through DLS to contain similar sized nanoparticles, primarily about 35 nm, showed some overlap, but produced a broader peak. This could again be explained by higher levels of aggregation present within this sample or it being a sample

of higher polydispersity. The UV-Vis spectrum for synthesis of silver nanoparticles with both gum arabic and citrate also may be understood with aid from corresponding DLS data and literature values, which point to silver nanoparticles between 50-60 nm in diameter. The small peak at 538 nm seen in the tannic acid silver nanoparticles is characteristic of aggregated, larger particles.

5.3: Dynamic Light Scattering Results

DLS measurements were taken at concentrations found by UV-Vis. Typically a target absorbance of 0.5 was set to ensure the best quality data. Samples were diluted by 4 parts water, 1 part silver nanoparticles if found to have absorbance values approaching 1 or greater prior to transfer into DLS. Samples with absorbance values below 0.1 were deemed too dilute for the DLS to generate an accurate model of particle sizing. This was not the case for any samples from the citrate reduced (5mM-10mM) silver nanoparticles taken at 35 minutes. The DLS provided three different graphical representations of data collected. Particle sizing is shown through the relative intensity readings of light scattered by particles of various hydrodynamic diameters, the relative number of particles of a diameter, and the relative total volume of particles of a certain diameter.

5.3.1: Comparison of Silver Nanoparticles Synthesized via Various Reducing Agents

The following graph's x-axis was adjusted to highlight the nanoparticle size range of interest, and values greater than 120 nm were omitted.
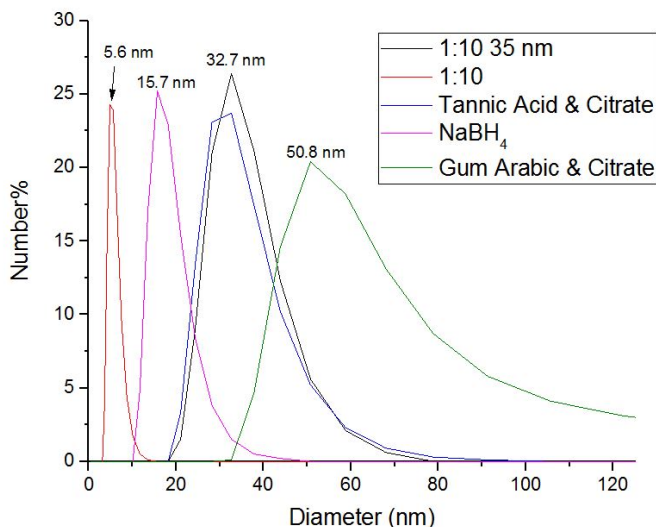
Figure 18: Number Readings from DLS Measurement of Silver Nanoparticles Synthesized from Various Reducing Agents

Synthesis using the reducing agents of both tannic acid and citrate, as well as the synthesis with 10 mM citrate alone which was indicated to have produced 35 nm particles show very similar peaks and polydispersity quantified by the variation in number%. Gum arabic has the broadest size range, and illustrates that gum arabic as a capping agent may not be ideal for synthesis of particles required to be between 30-50 nm; in other synthesis with gum arabic, 10 nm particles were produced. The 1:10 ratio that produced particles <10 nm has the tightest distribution; particles synthesized via this reaction of 10 mM sodium citrate, as well as with sodium borohydride, may not have been allowed to nucleate to the point of creating a broad size distribution. With the sodium borohydride reaction, it should be noted that large aggregates fell out of solution within a week after synthesis. It was predicted that the sodium borohydride reaction, as a strong reducing

agent, would produce small, monodisperse particles if stopped at the proper time as

reactant is consumed so rapidly, or large aggregates, which is in line with what was

observed.
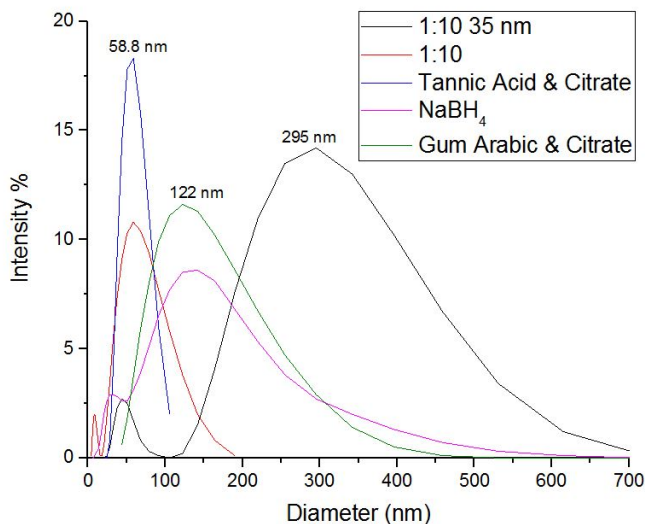
Figure 19: Intensity Readings from DLS Measurement of Silver Nanoparticles
Synthesized from Various Reducing Agents

The size distribution in terms of intensity tells a different story to that of size distribution

by number, as larger particles will inherently have a greater cross-sectional area,

scattering more light and may thus contribute to a relatively high percentages of the

intensity. The largest peak, that of tannic acid, indicates synthesis by tannic acid and

sodium citrate reducing agents produced nanoparticles with percentiles most within the

target range. The 1:10 citrate ratio of smaller sizes also appears to show adequate size

range by intensity, though the 1:10 citrate ratio purported to have produced particles with

35 nm diameters has a large peak at 300 nm, indicating that silver nanoparticle clusters

have likely arisen.
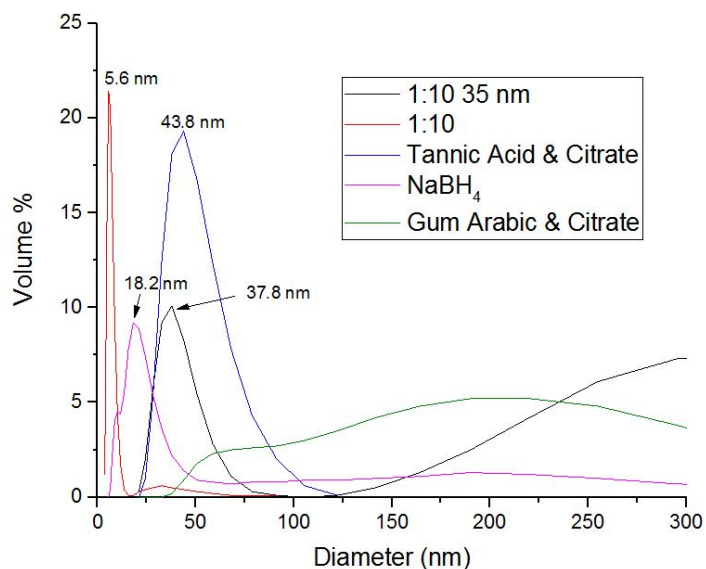
Figure 20: Volume Readings from DLS Measurement of Silver Nanoparticles Synthesized from Various Reducing Agents

By volume, the 1:10 citrate ratio which produced 10 nm particles, in red, once again appears to be a relatively more monodisperse distribution. Gum arabic again shows a wider size distribution, with larger, aggregated particles; most of this data was not shown in this graph as the focus was on particles <100 nm. Synthesis via tannic acid and citrate appears to have produced a higher percentage of its particles within the desired size range than other synthesis routes, also shown in the intensity data. A secondary peak for the 35 nm 1:10 silver NP exists at 342 nm, though its largest peak exists for a nanoparticle diameter of about 38 nm.

Reduction by sodium borohydride and gum arabic both showed aggregates of around 5 μm in diameter, or 5000 nm. The 1:10 citrate ratio of 35 nm silver NPs also contained a minute number of 5 μm particles according to volume and intensity readings, but no particles of this size were recorded by number readings.

56

5.3.2 Comparison of Nanoparticle Size and Dispersity of Various Ag:Cit Concentrations
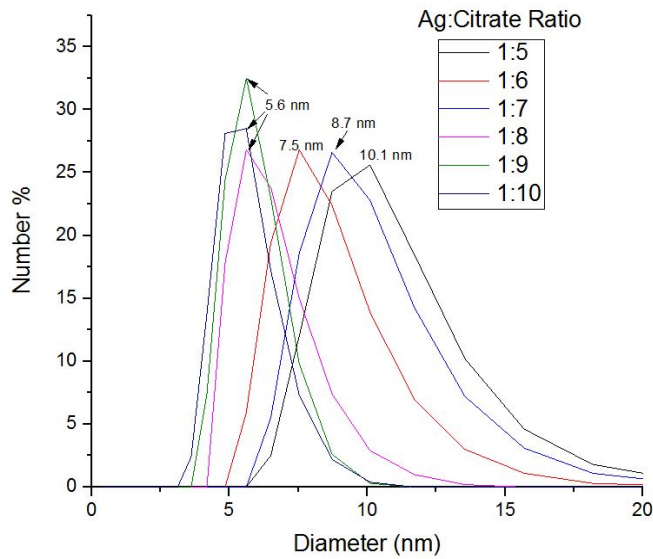
Figure 21: Silver Nanoparticle Size by Number at Varying Initial Concentrations of Citrate Reducing Agent
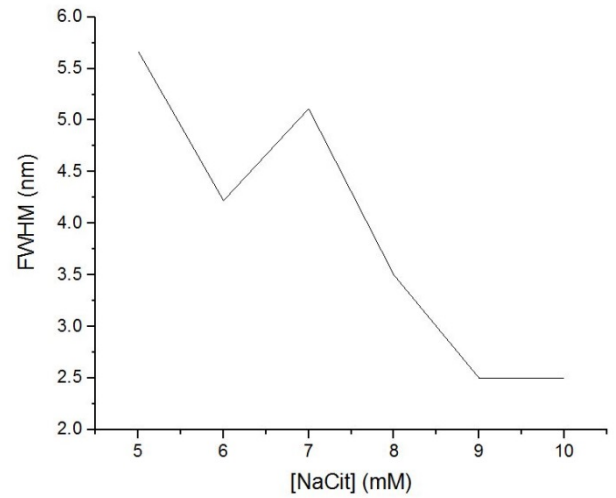
Figure 22: Size Distribution of Nanoparticles of Varying Initial Citrate Concentrations by value of the Full Width at Half Maximum

From analysis of the size distributions of varying citrate concentrations at 35 minutes into the reaction, it appears synthesis with higher citrate concentrations show less polydispersity. Figure 22 shows the loose correlation relating higher citrate concentration to lower values of the full width at half maximum (FWHM) of the Number% main peak. This was predicted, as higher citrate concentration may reduce aggregation, preventing silver nanoparticles from colliding and instead allowing growth through collision with reduced silver atoms.

5.3.3 Filtering and Centrifugation
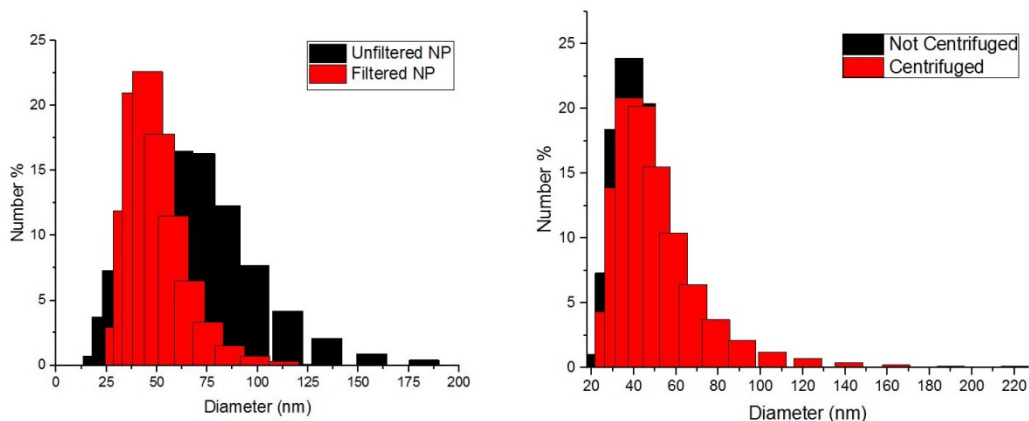
Figure 23: Size Distribution of Nanoparticles Before and After Separation Techniques, DLS measurements by Number%
Left: Syringe Filtering, Right: Centrifugation

Synthesis procedures for filtered and centrifuged silver solutions are in section 4.2, and involved using tannic acid and sodium citrate as reducing agents. It was determined both filtering nanoparticles by size exclusion and centrifugation methods are successful in improving the quality of a very polydisperse sol. The original polydisperse sol is shown in black in Figure 23, and was synthesized by reduction of silver nitrate by sodium citrate and tannic acid. The graph to the left shows a solution after filtering in red, while the graph to the right shows a solution after it was centrifuged in red. Although the currently available centrifuge and size exclusion syringe filters can produce a sol of moderate polydispersity from one of high polydispersity, the end product is unlikely to be a highly monodisperse sol within the desired size range if the initial sol already was of high polydispersity. A better size distribution may be produced from careful synthesis by chemical reduction than that from these methods.

5.4: Aggregation of Silver Nanoparticles

Aggregation of silver nanoparticles was a concern throughout this project. With each new reaction attempted, high temperatures and poorly performed technique had the potential to result in synthesis of aggregated particles with poor long-term stability. As the desired composite matrices require the long term

Figure24: Aggregated Silver Nanoparticles Fall Out of Solution

stability of silver nanoparticles within cellulose nanofibrils, aggregation as depicted in Figure 24 to the right in which nanoparticles have fallen out of solution would drastically reduce the usefulness of the product. Data samples became unusable as large time intervals between silver nanoparticle synthesis and subsequent experiments allowed aggregation to occur. The literature points to colloidal stability of nanoparticles of 10 nm, 50 nm, and 100 nm sizes for 7 weeks [25]. However, this assumes that the particles are electrostatically stabilized by a protective double layer. Observed aggregation could occur within a couple weeks for an otherwise stable appearing sample of 1:10 silver nanoparticles.

5.5: Transmission Electron Microscopy Results

TEM images were analyzed using the imaging analysis software ImageJ such that particle sizes could be determined through analysis of the particle widths in respect to the provided scale bar. ImageJ is an imaging tool capable of converting a length in pixels to a SI unit of length. ImageJ analysis began with opening the TEM image files of each of the silver nanoparticle reactions with varying citrate concentrations. The scale bar provided in each TEM image was used as a known length which ImageJ then converted into a length in number of pixels. The diameter of nanoparticles within the image could then be calculated through the conversion of pixels to distance, but not before background noise

was filtered from the image and the nanoparticle boundaries better defined. Filtering combined an understanding of the size range one might expect with an educated guess from observation of the TEM image; expected particle size from DLS was considered.

Nanoparticles overlapping in the image may have been difficult to distinguish. The TEM image is limited in its ability to consistently capture the full range of particle sizes. If the instrument height is optimized to capture images of NPs of 100 nm diameter, it was observed that smaller particles, with 10 nm diameter for example, were out of focus and did not appear in some images. Additionally, because of the low concentration of nanoparticles in solution, there was great difficulty in locating nanoparticles for imaging. Because of this, both nanoparticle solutions with initial citrate concentrations of 6 mM and 7 mM show poor data, and the 6 mM TEM was not included for statistics.

Visual comparison of the original TEM images with the resulting filtered image was done prior to calculation of ImageJ object diameters, as shown below in Figure 25 in an attempt to produce more accurate particle sizing from TEM images. These diameters were then compared to size numbers for nanoparticle diameters obtained from the DLS.
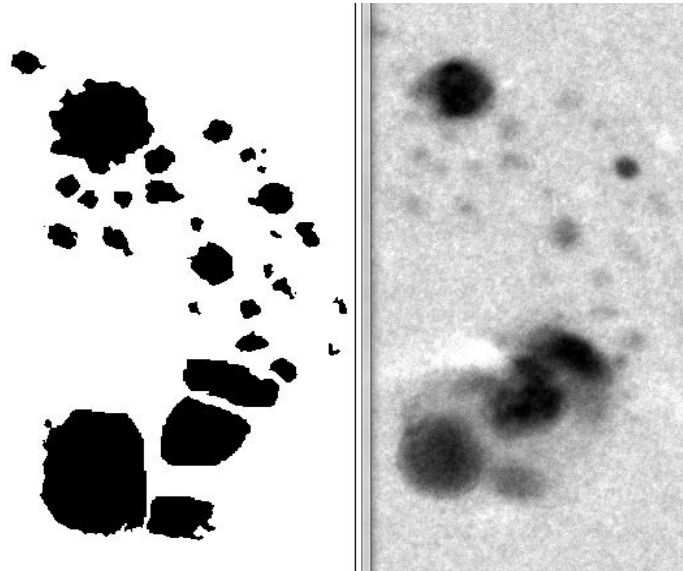
Figure 25: Comparison of Silver Nanoparticles Synthesized by 1:5
Ag:Citrate Enhanced within ImageJ software with raw TEM Images

Objects of up to 12 pixels were removed from the image. This was intended to remove noise from the TEM image, leaving only objects that were nanoparticles. The resulting histograms show a loose trend that the lower citrate concentrations show heterodisperse particle sizing, while 9 and 10 mM citrate recipes show more monodisperse size distributions without large particles greater than 60 nm in diameter. 1:7 and 1:8 ratios are of questionable data quality and were not considered to definitively support DLS data, though the data loosely falls between that of the 1:5 and 1:10 ratios. Artifacts from TEM images and noise are likely responsible for some data indicating the presence of nanoparticles <5 nm, as with the high count number in the 1:8 ratio.

5.5.1: Silver Nanoparticles Synthesized with Sodium Citrate

When the image was analyzed using ImageJ, the size of the particles were found to mostly be around 10 nm, which was approximately what was seen in DLS results. The below TEM image of 1:10 citrate ratio was used to determine approximate sizes of

61

nanoparticles synthesized. Highlighted in bright green are a number of particles, with diameters ranging from approximately 5-50 nm.
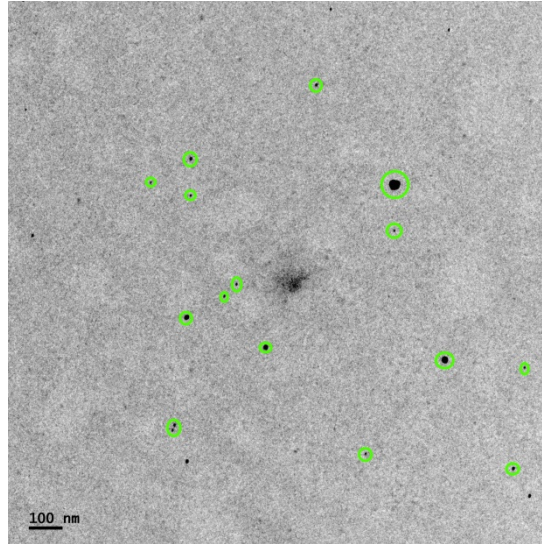
Figure 26: TEM Image of Silver Nanoparticles Synthesized with 10mM Citrate Reducing Agent

TEM images of the nanoparticles resulting from the 1:6 ratio of silver nitrate to sodium citrate lacked sample size as well as the size distribution found in DLS data. Nanoparticles were difficult to find as the concentration of nanoparticles was low. Additionally, adjusting the TEM instrument to view one size of particle may result in other sizes of particles becoming out of focus. This narrows the size distribution seen in analysis of TEM.
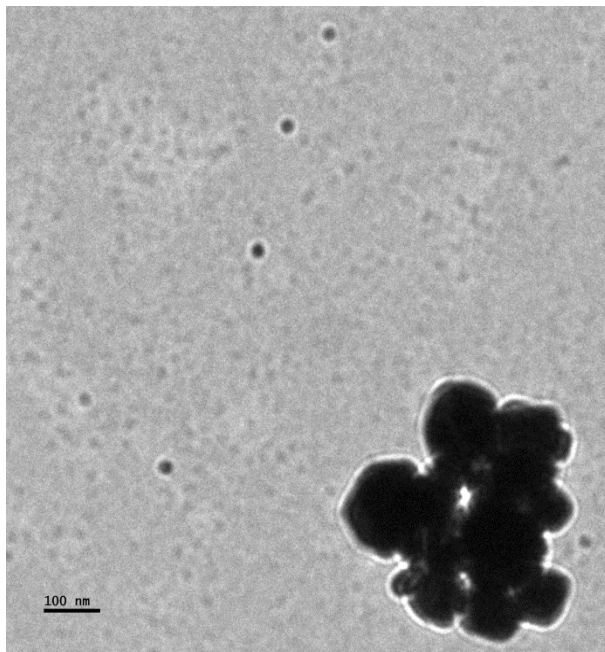
Figure 27: TEM of Aggregated Silver Nanoparticles Synthesized via 5mM Citrate Reducing Agent
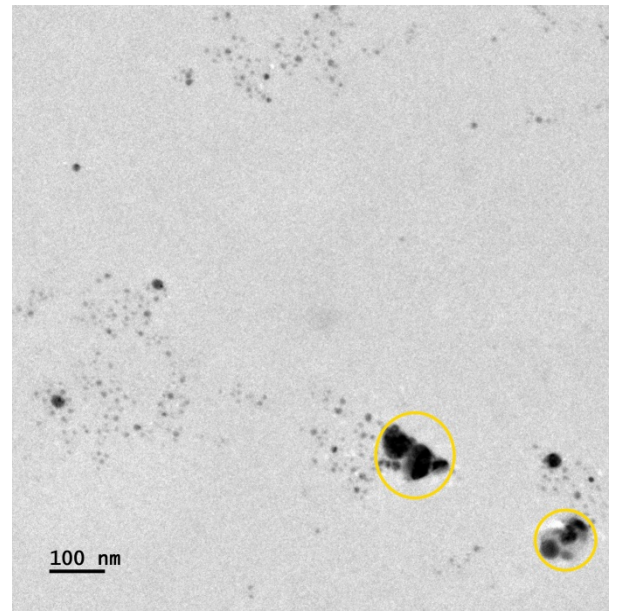
Figure 28: TEM Image of Silver Nanoparticles Synthesized via 5mM Citrate Reducing Agent

Although nanoparticle clusters were seen in all ratios, the aggregation was most prominent in the 1:5 and 1:6 ratios. These ratios produced micron scale clusters. Particle clusters of this size are undesirable for SERS enhancement. SERS enhancement is proportional to particle size, but a monodisperse sol would give the most useful information, as it could be used to determine the concentration of target molecule present, and if that concentration was at a permissible level. Clustered silver nanoparticles would waste chemicals, as dispersion into CNF would be poor. Given equal starting material, a silver sol of smaller sizes, if properly dispersed, would be more capable of covering greater surface area for enhancement.

Figure 29: Number of Particles <40nm by Size for 1:5 to 1:10 Ag:Citrate Silver Nanoparticle Synthesis at 35 minutes from TEM
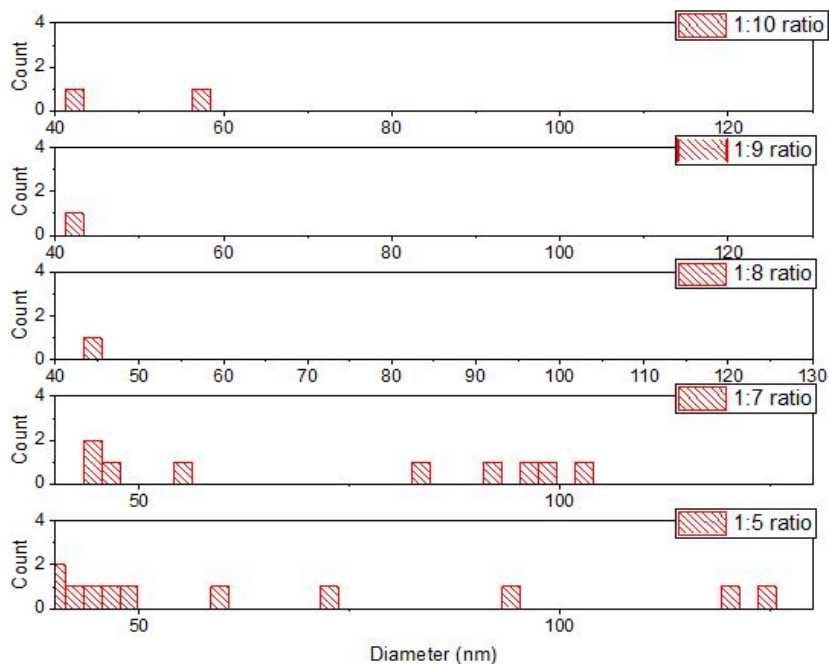
Figure 30: Number of Particles >40nm by Size for 1:5 to 1:10 Ag:Citrate Silver Nanoparticle Synthesis at 35 minutes from TEM

TEM of 1:5 and 1:10 ratios are the best data of the various citrate concentrations. As supported in DLS measurements, the 1:5 ratio shows the greatest polydispersity, with some particle aggregates large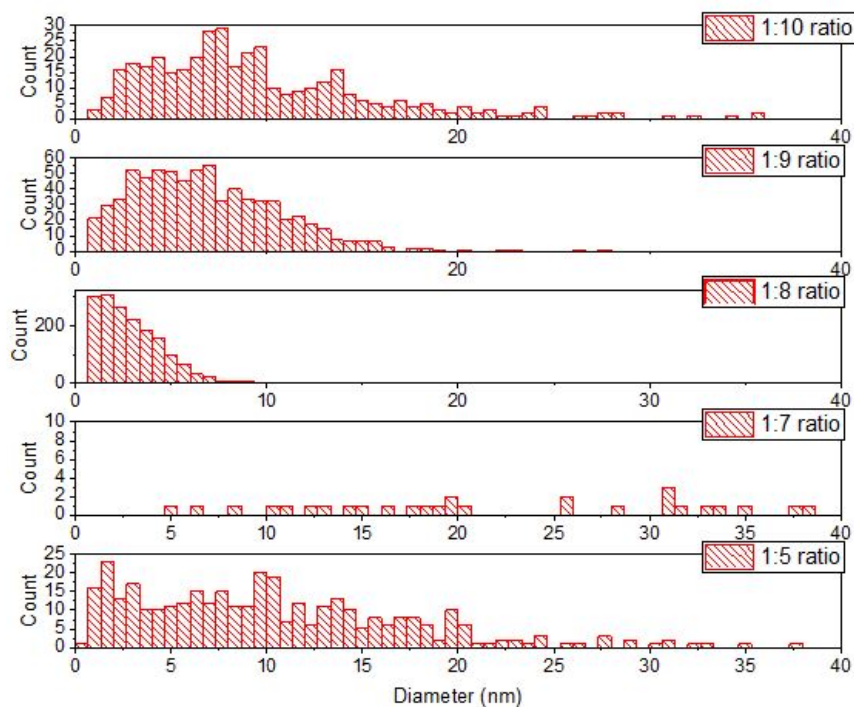r than 100 nm. The 1:10 ratio produced some particles within the 30-50 nm range, but most particles were approximately 10 nm in diameter.

5.5.2: Silver Nanoparticles and CNF

TEM was taken of a very dilute solution containing CNF and silver nanoparticles. A 300 time dilution of CNF at 3wt% was made, diluted with aqueous silver nanoparticle solution synthesized by the 1:10 Ag:NaCit synthesized nanoparticles. Particles of ~50 nm appear to associate with cellulose nanofibrils. These nanoparticles do not appear to be entrained within the fibrils, but one might imagine the silver nanoparticles to be of an adequate size. There is little uniformity in the size of the spacing between fibrils; rather, one might imagine a range of sizes might be capable of entrainment within a CNF composite matrix, though long-term stability of such particles may be of concern.

Figure 31: TEM of ~50 nm Silver Nanoparticles in dilute CNF solution

5.6: Raman Spectra
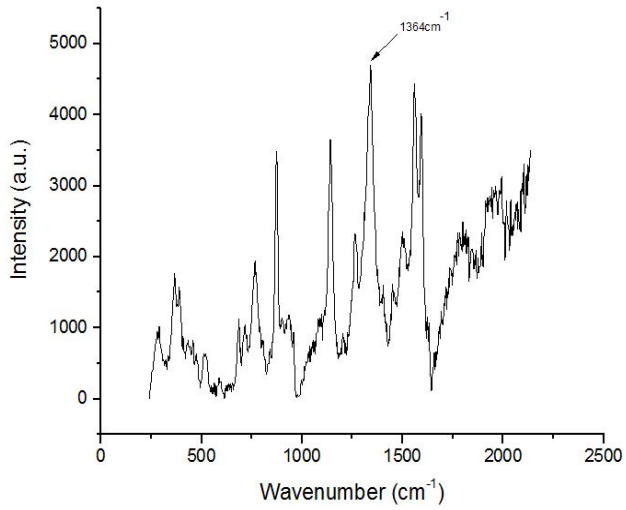
Figure 32: Raman Spectra for Crystal Violet taken in collaboration with Muhammad Hossen
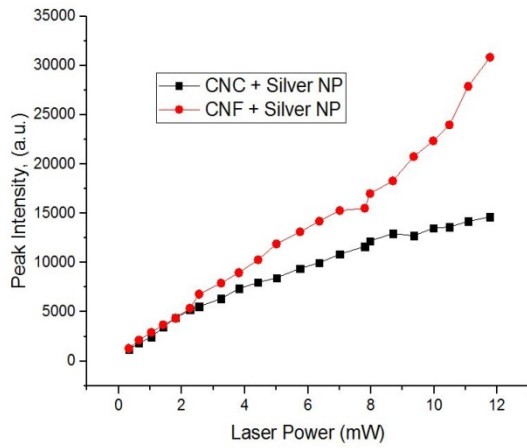
Figure 33: SERS Enhancement Comparison between Silver NPs in CNC and CNF at Various Laser Powers taken in collaboration with Muhammad Hossen
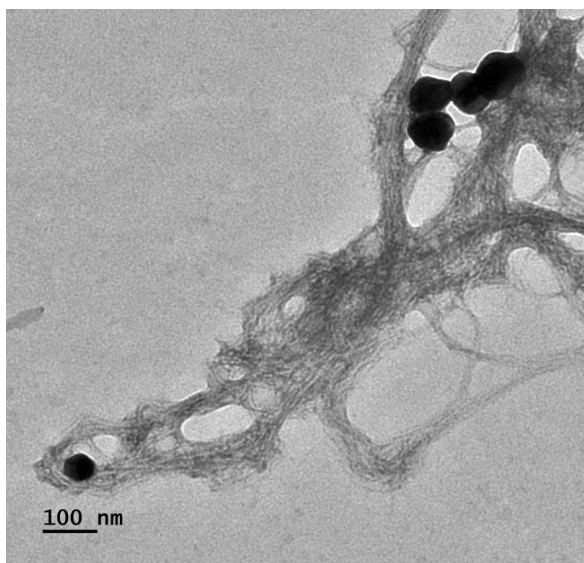
The Raman spectrum shows the Raman shift peaks for crystal violet. Upon excitation by a 532 nm laser, emitted photons exhibited frequency shifts of values corresponding to wavenumbers (cm^{-1}) along the x-axis with intensities (a.u.) given by the y-values. A peak at approximately $1364 cm^{-1}$ corresponding to N-phenyl stretching of the crystal violet molecule [38], was chosen for further analysis as it was the highest intensity peak. Comparison of signal enhancement by silver nanoparticles in CNC and CNF composite matrices were taken at this wavelength; as the laser power was increased, it became clear that the silver-CNF composite matrix was capable of greater signal enhancement.

5.7: Porosity

Figure 34 shows that within the patent pending drying setup of porous blocks, porosity decreases as the CNF slurry is dried over time starting from a porosity of 97%. As time passes, the pores within a CNF composite matrix become smaller, making it difficult for silicone oil to gain access to all the pores in sample removed at later times from the drying setup. As such the left side of the graph is theoretically more accurate than the right, which includes data taken at later times.
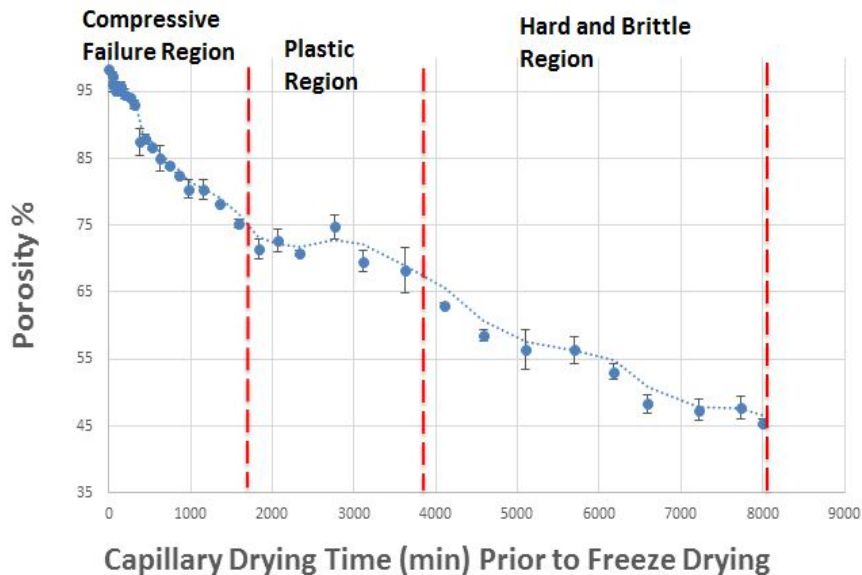
Figure 34: Porosity Measurement of Silver Nanoparticles-Cellulose Nanofibrils Composite matrix Using Silicone Oil Method, data collected in collaboration with Muhammad Hossen

The plastic region is perhaps the most easily characterized, as it reaches a balance for both easy handling and ease in which Silicone oil gains access to its pores. This data may be used to optimize porosity for Raman signal. Samples containing silver nanoparticles dried under the specified constant conditions and taken at various time intervals corresponding to a range of porosities given in the graph will be used as Raman substrates, and later compared for SERS enhancement. This may then indicate a porosity at which the synthesized silver nanoparticles are best engineered for greatest surface coverage and dispersion.

5.8: Scanning Electron Microscopy

As CNF is a non-conducting material, and as such special measures discussed in the Background Section were taken to elucidate silver nanoparticles at the surface of CNF. SEM imaging was also made more challenging due to the low concentration of silver nanoparticles. These images revealed that silver nanoparticles of similar sizes were

clumping together on the CNF surface. This was suggested to be because of Van der Waals forces.

Figure 35: SEM of the Silver Nanoparticles of varying sizes at the surface of a CNF composite matrix

Particles of two size ranges are shown circled in teal and red. The Van der Waals force is likely responsible for like-particles clumping together on the CNF surface. It is anticipated that adjustment of pH will solve this problem.

Figure 36: SEM of the Silver Nanoparticles of varying sizes at the surface of a CNF composite matrix

Medium range nanoparticles highlighted with a red circle happen to appear better dispersed in the SEM image. The large particles circled in green are not entrapped by cellulose nanofibrils, though they appear associated with or adsorbed to the surface of CNF. The image may not be resolved well enough to determine if any nanoparticles circled in red are entrained.

5.9: pH and Zeta Potential Optimization

In maximizing pH, the effective charge repulsion between particles is maximized, perhaps in addition to the surface energy to a value at which the nanoparticles are most stable [21]. The first experiment of zeta potential conducted utilized sodium hydroxide as a strong base and 5% acetic acid, a weak acid, to adjust the pH of the sol. Due to concern that the base's strength may be affecting our understanding of the system, two further experiments were conducted. One approached the problem by introducing no new chemical species, but rather adding addition sodium citrate after the reaction had completed. The citrate ion results in a weak base, slowly raising the pH of the solution as more is added. This method is both limited by the screening effect and the solubility constant of sodium citrate. Due to high uncertainty in zeta potential measurements and this particular experiment only having been performed once, there is little to be said of a trend.

The experiment of pH and zeta optimization using sodium citrate was performed with silver nanoparticles from a 1:10 Ag:Cit synthesis which produced particles of approximately 10 nm. With sodium citrate as the only chemical added, it appears that upon completion of the double layer, the screening effect quickly surpasses any

additional stability in additional sodium citrate, causing nanoparticles to fall out of solution. For this reason the nanoparticles fall out of solution before a pH of 8 can be reached by addition of sodium citrate. The literature indicates that nanoparticles of varying size may behave differently [23], and thus further experimentation is required to gain full understanding of the system as well as to provide adequate statistics. The literature points to 100 nm particles reaching greater stability [23], which contrasts with observations made, as large particles were often seen to fall out of solution more rapidly than aggregation of silver NP solutions containing smaller particles. The literature might be explained by citrate ions more readily forming a double layer on larger particles as they may not be in as close proximity to other citrate ions' repulsive charges on the surface of the same particle [23]. It should be noted that the measurements of zeta potential in the literature, in addition to those made in experiments, follow poor correlations, if any may be made. It is from a combination of observation and zeta potentials that one may indicate slightly basic pH values as providing greater stability.

The deionized water was found to be at a neutral pH of approximately 7, as 10 mL was tested using the pH meter. Upon the addition of both sodium citrate and silver nitrate solutions, the pH rose to a more basic 7.2. After the reaction, with zeta potential data from the adjustment of pH, it was concluded that a more basic pH granted the system better stability. With only sodium citrate, a pH of approximately 7.3 was found to be a turning point in the stability of the solution. At a pH of 7.3, the colloidal system had the most negative zeta potential, the extrema previously discussed. Solutions above the pH 7.3, or adding more sodium citrate to increase pH, resulted in less negative zeta potentials, meaning that the repulsive forces had less effect, and the screening effect

71

began to dominate. The negative charges felt were less negative, due to the presence of the sodium ion. This effect arising from presence of sodium ion will be true for all experiments in adjustment of pH, but the screen effect was a greater concern in adjustment by sodium citrate. Sodium citrate was needed in greater amounts compared to sodium bicarbonate or sodium hydroxide in order to adjust the pH. The surface energy and thus surface tension by which the silver nanoparticles are held together may experience changes with pH adjustment. Figure 37 shows the results of silver nanoparticle solution pH control by addition of sodium citrate as well as control by addition of sodium bicarbonate. As the magnitude of zeta potential increases, so does the stability of the solution. Further tests may yield an optimal system for stability.
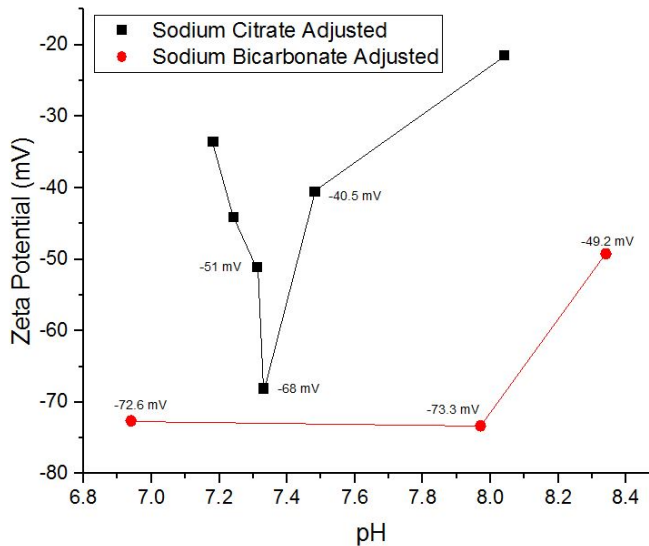
Figure 37: Dependence of Zeta Potential and Stability on pH, adjustment by adding Sodium Citrate or Sodium Bicarbonate
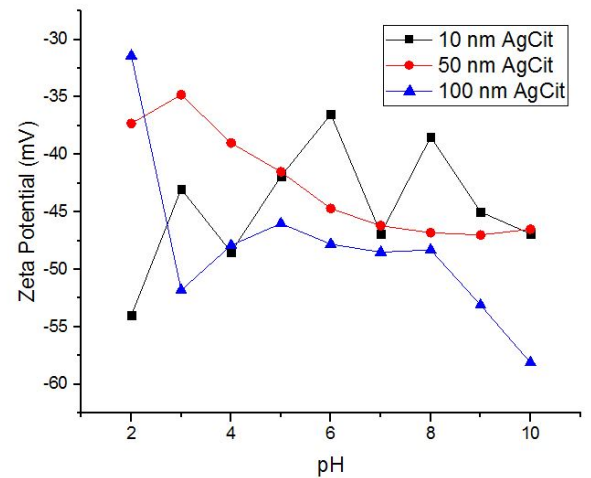
Figure 38: Dependence of Zeta Potential and Stability on pH, Literature Values for 10 nm, 50 nm, and 100 nm Citrate Reduced Silver NPs [23]

Chapter 6: Conclusions and Future Progress

A reproducible, monodisperse size distribution of desired size range between 30-50nm silver nanoparticles continues to be difficult to synthesize. However, one may find

that with careful selection of reaction parameters including reducing agent, temperature, and time, control over nanoparticle size is possible. Although time consuming, investigating parameters will likely yield a set of optimal reaction conditions that would be ideal for obtaining monodisperse silver nanoparticles of any size range, as nanoparticles synthesized by methods within this paper showed a large potential range. Gum acacia as reducing agent alone is too weak to successfully produce monodisperse nanoparticles. Conversely, sodium borohydride is too strong a reducing agent. Both tannic acid and sodium citrate are considered to be reducing agents with desirable reduction potential. Currently the 1:10 Ag:Citrate synthesis shows the most promising control in its monodispersity and simplicity for Raman characterization.

Preliminary data shows the silver nanoparticle solutions have improved stability at slightly basic pHs, with excess sodium citrate or sodium bicarbonate added after completion of synthesis. Sodium borohydride was more effective in altering pH than sodium citrate, as pH was successfully adjusted over a greater range without particles falling out of solution due to the screening effect present with the addition of sodium ion of either sodium citrate or sodium bicarbonate. As stated further tests are necessary to determine a pH at which greatest stability may be obtained.

Sigma Aldrich prices 40nm silver nanoparticles as more expensive than both 20nm and 60nm particles; this may be due to the difficulty in timing and reproducibility to halt the reaction at the proper time to produce particles of this size [39]. Although speculative, reduction by sodium citrate may follow a similar pattern to that found with sodium borohydride, but at a slower rate. This pattern was that stability is found at a small size range, perhaps 10 nm, and larger sizes of over 60nm [8]. The growth of silver

nanoparticles between these size ranges may encounter varying levels of stability or meta-stability, and depending upon the reducing agent and electrostatics of the system, various particle sizes may exist as transient states [8].

Silver nanorods, having a higher aspect ratio, may produce greater signal enhancement; it was predicted that they are capable of producing a greater electromagnetic field. Shape is considered due to the importance of an electromagnetic field's orientation. Difficulties in proper orientation could reduce the effectiveness of the SERS effect with these rod shaped nanoparticles. Silver nanowire arrays are also of interest for signal enhancement, and would also potentially produce greater signal enhancement [39].

A better setup for the controlled synthesis of silver nanoparticles by the addition of a thermistor into the round bottom flask would be a simple improvement. Thermistors are small sensors which produce a resistance inversely proportional to temperature. This would be a great improvement over the thermometer. Currently if the temperature of the hot plate is changed, there is an unknown time delay for the oil bath, round bottom flask, and reacting solution to reach an approximate thermal equilibrium. With the addition of the thermistor, one could monitor the instantaneous temperature within the reaction vessel, as the thermometer does not fit into the closed system. The operating temperature range of Honeywell thermistors, -60°C to 300°C, would be well within our procedural temperatures [40]. The hot plate could also be improved, as both the temperature and stirring controls are analog on the current model used. Although the hot plate has an analog control, the temperature readings are in multiples of 5. A digital control for stirring would likely increase reproducibility.

Integrating the silver nanoparticle solution into the mass colloider during an early stage of the cellulose nanofiber synthesis may be necessary to achieve better dispersion. Currently the 3wt% slurry is hand mixed with deionized water or silver nanoparticle solution before being brought to the drying setup.

Works Cited

[1] WHO/UNICEF, "Progress on sanitation and drinking water- 2015 Update and MDG Assessment," in *UNICEF and World Health Organization 2015*, Geneva, 2015.

[2] Millenium Ecosystem Assesment, "Ecosystems and Human Well-Being: Synthesis," in *Millenium Ecosystem Assessment*, Washington, DC, 2005.

[3] K. Fischer, E. Fries, W. Korner, C. Schmalz and C. Zwiener, "New developments in the trac analysis of organic water pollutants," *Applied Microbiology Biotechnology,* no. 94, p. 19, 2012.

[4] Z. Movasaghi, S. Rehman and I. U. Rehman, "Raman Spectroscopy of Biological Tissues," *Applied Spectroscopy Reviews,* vol. 42, no. 5, 2007.

[5] P. Stiles, J. Dieringer, N. Shah and R. Van Duyne, "Surface-Enhanced Raman Spectroscopy," *Analytical Chemistry,* p. 29, 2008.

[6] G. Li, M. Chen and T. Wei, "Application of Raman Spectroscopy to Detecting Organic Contaminant in Water," in *IITA International Conference on Control, Automation and Systems Engineering*, 2009.

[7] A. Cooper, Biophysical Chemistry, Cambridge: The Royal House of Chemistry, 2011.

[8] E. Alarcon, M. Griffith and K. Udekwu, Silver Nanoparticle Applications In the Fabrication and Design of Medical and Biosensing Devices, Springer International Publishing, 2015.

[9] F. Jiang and Y.-L. Hsieh, "Synthesis of Cellulose Nanofibril Bound Silver Nanoprism for Surface Enhanced Raman Scattering," *Biomacromolecules,* vol. 15, no. 10, pp. 3608-3616, 2014.

[10] H. Yano, "Production of cellulose nanofibres and their applications," *International Polymer Science and Technology,* vol. 40, no. 7, 2013.

[11] R. Li and a. et, "Quantitative analysis of crystal violet by Raman spectroscopy," *Spectroscopy,* 2012.

[12] J. Moore, C. Stanitski and P. Jurs, Chemistry: The Molecular Science, Mason: Cengage Learning, 2012.

[13] "Silver oxide," Sigma-Aldrich, 2016. [Online]. Available:
http://www.sigmaaldrich.com/catalog/product/aldrich/226831?lang=en&region=US.
[Accessed 14 February 2016].

[14] A. Khalil, "Green composite matrices from sustainable cellulose nanofibrils: A
review," *Carbohydrate polymers,* vol. 87, no. 2, 2012.

[15] Nikkei Asian Review, "Material of the future: Japanese paper makers to mass
produce cellulose nanofiber," Nikkei, Inc., Tokyo, 2016.

[16] The University of Maine, "The Process Development Center: Facilities Available for
Use- Nanocellulose Facility," The University of Maine, Orono.

[17] X. Xu, F. Liu, L. Jiang, J. Zhu, D. Haagenson and D. Wiesenborn, "Cellulose
Nanocrystals vs. Cellulose Nanofibrils: A Comparative Study on Their
Microstructures and Effects as Polymer Reinforcing Agents," *Applied Materials and
Interfaces,* vol. 5, pp. 2999-3009, 2013.

[18] H. Youssef, "Cellulose nanocrystals: chemistry, self-assembly, and applications,"
Chemical Reviews, vol. 110, no. 6, 2010.

[19] G. Truskey, F. Yuan and D. Katz, Transport Phenomena in Biological Systems,
Pearson, 2009.

[20] K. Mullen, "Darcy's Law," National Ground Water Association, 5 September 2012.
[Online]. Available: http://www.ngwa.org/Fundamentals/teachers/Pages/darcy-
law.aspx. [Accessed 25 March 2016].

[21] D. Shaw, Introduction to Colloid and Surface Chemistry, Woburn: Reed Educational
and Professional Publishing Ltd., 1992.

[22] Malvern Instruments, "Zeta Potential," Malvern Instruments, Ltd., 2016. [Online].
Available: http://www.malvern.com/en/products/measurement-type/zeta-potential/.
[Accessed 29 March 2016].

[23] nanoComposix, "Tech Note: Zeta/pH Curves and Isoelectric Point Data for Standard
nanoComposix Silver Citrate and PVP Nanoparticle Dispersions," nanoComposix,
San Diego, 2012.

[24] P. Debye and H. E, "On the Theory of Electrolytes," *Physikalische Zeitschrift,* vol.
24, no. 9, pp. 185-206, 1923.

[25] N. Bastus, F. Merkoci, J. Piella and V. Puntes, "Synthesis of Highly Monodisperse Citrate-Stabilized Silver Nanoparticles of up to 200 nm: Kinetic Control and Catalytic Properties," *Chemistry of Materials,* vol. 26, pp. 2836-2846, 2014.

[26] H. Li, H. Xia, W. Ding, Y. Li, Q. Shi, D. Wang and X. Tao, "Synthesis of Monodisperse, Quasi-Spherical Silver Nanoparticles with Sizes Defined by the Nature of Silver Precursors," *Langmuir,* vol. 30, pp. 2498-2504, 2014.

[27] C. Dong, X. Zhang, H. Cai and C. Cao, "Facile and one-step synthesis of monodisperse silver nanoparticles using gum acacia in aqueous solution," *Journal of Molecular Liquids,* vol. 196, pp. 135-141, 2013.

[28] S. Sally, B. Mozghan, A. Jeyarajasingam, S. Rutkowski and C. Boritz, "Systhesis and Study of Silver Nanoparticles," Journal of Chemical Education, Philidelphia, 2007.

[29] T. Tsuji and a. et, "Preparation of silver nanoparticles by laser ablation in polyvinylpyrrolidone solutions," *Applied Surface Science,* vol. 254, no. 16, pp. 5224-5230, 2008.

[30] "SpectraSchool," Royal Society of Chemistry, 2015. [Online]. Available: http://www.rsc.org/learn-chemistry/collections/spectroscopy/introduction#IRSpectroscopy. [Accessed 17 March 2015].

[31] "Dynamic Light Scattering: An Introduction in 30 minutes," Malvern Instruments, DLS Technical Note.

[32] T. Pradeep, Nano: The Essentials, Understanding Nanoscience and Nanotechnology, Tata McGraw-Hill Educaiton, 2007.

[33] "Transmission Electron Microscope-A Basic Look How TEMs Work," AZoNano, 11 June 2013. [Online]. Available: http://www.azonano.com/article.aspx?ArticleID=1723. [Accessed 18 March 2015].

[34] E. Fischer, B. Hansen, V. Nair, F. Hoyt and D. Dorward, "Scanning Electron Microscopy," in *Current Protocols in Microbiology*, 2012.

[35] T. Dadosh, "Synthesis of uniform silver nanoparticles with a controllable size," *Materials Letters,* vol. 63, pp. 2236-2238, 2009.

[36] D. Steinigeweg, "Fast and cost-effective purification of gold nanoparticles in the 20-

250 nm size range by continuous density gravity centrifugation," *Small,* vol. 7, no. 17, 2011.

[37] J. Kaushik and R. Bhat, "Why Is Trehalose an Exceptional Protein Stabliizer? An Analysis of the Thermal Stability of Proteins in the Presence of Compatible Osmolyte," *The Journal of biological chemistry,* 2003.

[38] E. Liang, X. Le and W. Kiefer, "Surface-Enhanced Raman Spectroscopy of Crystal Violet in the Presence of Halide and Halate Ions with Near-Infrared Wavelength Excitation," *The Journal of Physical Chemistry,* vol. 40, no. 10, pp. 7330-7335, 1997.

[39] Sigma-Aldrich Co. LLC, "Silver Nanoparticles: Properties and Applications," Sigma-Aldrich Co. LLC, 2016. [Online]. Available: http://www.sigmaaldrich.com/materials-science/nanomaterials/silver-nanoparticles.html. [Accessed 3 April 2016].

[40] Honeywell, "Temperature Sensors, Probes and Thermistors," Honeywell, 2016. [Online]. Available: http://sensing.honeywell.com/products/temperature-sensors?Ne=2308. [Accessed 6 September 2015].

Author's Bio

Matthew Talbot was born in Blue Hill, Maine, on April 18th 1994. He was raised in East Machias, Maine, and graduated from Washington Academy in 2012. During his four years at the University of Maine, Matt was enrolled as part of the Honors College, majored in Bioengineering, and attained minors in Nanotechnology and Pre-Medical Studies. As a sophomore he was extended a bid to join Phi Sigma Pi National Honor Fraternity, which he accepted. His senior year he was invited to and joined both Phi Kappa Phi Honor Society and Tau Beta Pi Engineering Honor Society.

Upon graduation Matt plans to hike the Appalachian Trail and then contribute to the field of Bioengineering, expanding the knowledge he received from his education at the University of Maine.